Inorganic Chemistry

Article

pubs.acs.org/IC

Biologically Relevant Heterodinuclear Iron−Manganese Complexes

Michaël Carboni,[†] Martin Clémancey,[†] Florian Molton,[‡] Jacques Pécaut,[§] Colette Lebrun,[§] Lionel Dubois,[§] Geneviève Blondin,*[,†] and J.-M. Latour*[,†]

[†]Laboratoire de Chimie et Biologie des Métaux-pmb, UMR 5249, Université Joseph Fourier—Grenoble 1/CEA-DSV-iRTSV/CNRS, Grenoble F-38054, France

[§]Laboratoire de Reconnaissance Ionique et Chimie de Coordination, UMR-E 3, CEA-INAC-SCIB/Université Joseph Fourier—Grenoble 1/CNRS, Grenoble F-38054, France

[‡]Département de Chimie Moléculaire, UMR-5250, Université Joseph Fourier—Grenoble 1/CNRS, and Laboratoire de Chimie Inorganique Redox, Institut de Chimie Moléculaire de Grenoble, FR-CNRS-2607, BP-53, 38041 Grenoble Cedex 9, France

Supporting Information

ABSTRACT: The heterodinuclear complexes $[Fe^{III}Mn^{II}(L\text{-}Bn)(\mu\text{-}OAc)_2](ClO_4)_2$ (**1**) and $[Fe^{II}Mn^{II}(L\text{-}Bn)(\mu\text{-}OAc)_2](ClO_4)$ (**2**) with the unsymmetrical dinucleating ligand HL-Bn {[2-bis[(2-pyridylmethyl)aminomethyl]]-6-[benzyl-2-(pyridylmethyl)-aminomethyl]-4-methylphenol} were synthesized and characterized as biologically relevant models of the new Fe/Mn class of nonheme enzymes. Crystallographic studies have been completed on compound **1** and reveal an $Fe^{III}Mn^{II}\mu$-phenoxobis(μ-carboxylato) core. A single location of the Fe^{III} ion in **1** and of the Fe^{II} ion in **2** was demonstrated by Mössbauer and ^{1}H NMR spectroscopies, respectively. An investigation of the temperature dependence of the magnetic susceptibility of **1** revealed a moderate antiferromagnetic interaction (J = 20 cm^{-1}) between the high-spin Fe^{III} and Mn^{II} ions in **1**, which was confirmed by Mössbauer and electron paramagnetic resonance (EPR) studies. The electrochemical properties of complex **1** are described. A quasireversible electron transfer at −40 mV versus Ag/AgCl corresponding to the $Fe^{III}Mn^{II}/Fe^{II}Mn^{II}$ couple appears in the cyclic voltammogram. Thorough investigations of the Mössbauer and EPR signatures of complex **2** were performed. The analysis allowed evidencing of a weak antiferromagnetic interaction (J = 5.72 cm^{-1}) within the $Fe^{II}Mn^{II}$ pair consistent with that deduced from magnetic susceptibility measurements (J = 6.8 cm^{-1}). Owing to the similar value of the Fe^{II} zero-field splitting (D_{Fe} = 3.55 cm^{-1}), the usual treatment within the strong exchange limit was precluded and a full analysis of the electronic structure of the ground state of complex **2** was developed. This situation is reminiscent of that found in many diiron and iron−manganese enzyme active sites.

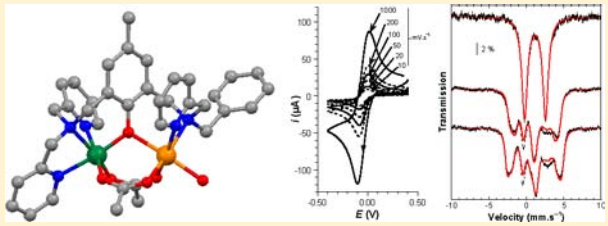

INTRODUCTION

Carboxylate-bridged diiron centers constitute the active site of many enzymes involved in dioxygen activation: ribonucleotide reductases (RNRs),[1,2] methane and toluene monooxygenases,[3,4] and Δ9-desaturase.[5] They are even present in a few hydrolytic enzymes, among which mammalian purple acid phosphatases are the most well-known.[6] The functioning of these sites is now reasonably well understood owing to numerous crystallographic and spectroscopic studies of the enzymes as well as the study of many biomimetic complexes.[7] It was found almost 2 decades ago that purple acid phosphatases from sweet potato possessed three isoforms differing by their dimetal active centers.[8] Interestingly, in addition to the classical $Fe^{III}Fe^{II}$ and $Fe^{III}Zn^{II}$ centers found in mammalian and red kidney bean enzymes, a new $Fe^{III}Mn^{II}$ center was discovered and structurally characterized.[9] All of these enzyme forms associate a ferric center to a M^{2+} ion, whose role is to bind the substrate. While metal substitution appears to be rather common in hydrolytic enzymes, it is definitely less frequent in redox enzymes, where the specific redox potential of a given metal is most often crucial to the biological activity.[10] In this respect, the recent discovery of a new family of RNRs functioning with such an iron−manganese site was striking.[11]

Class I RNRs contain two nonidentical dimeric subunits, R1 and R2, arranged as a R1R2 heterodimer.[2] Subunit R2 harbors a diiron center, and ribonucleotide reduction is performed by an active cysteine within the R1 subunit. The reactivity is initiated by the formation of a tyrosyl radical in subunit R2 by the reaction of the reduced diiron center with dioxygen.[1] It was found that *Chlamydia trachomatis* RNR-R2 protein, which lacks the canonical tyrosine, possesses an iron−manganese cofactor that replaces the tyrosyl radical when the reduced $Fe^{II}Mn^{II}$ enzyme is oxidized to the $Fe^{III}Mn^{IV}$ state by dioxygen.[11] Very recently, another iron−manganese cofactor was found in a RNR-R2 homologue (R2lox) from *Mycobacterium tuberculosis*.[12] This protein exhibits in the vicinity of the iron ion an unprecedented tyrosine−valine cross-link that results from a two-electron oxidation probably catalyzed by the metal center. These recent findings thus illustrate the possibility for these

Received: August 6, 2012
Published: September 18, 2012

iron−manganese centers to be involved in one- or two-electron oxidations, possibly using tyrosine as a cofactor.

Biomimetic diiron complexes have contributed heavily to an improved understanding of the dioxygen activation by diiron centers.[7] By contrast, corresponding models for the iron−manganese active centers are largely underdeveloped.[10] Indeed, only a few such complexes have been reported so far.[13−21] They were based very often on phenolate binucleating ligands, designed to investigate the magnetic properties of the dinuclear unit, and possessed generally a $Fe^{III}Mn^{II}$ unit.[13,15,17−20] Moreover, in most cases, these ligands saturated the coordination of both metals, thereby limiting the potential reactivity of the systems.[20] Very recently, Nordlander et al.[22] reported a new $Fe^{III}Mn^{II}$ complex from an unsymmetrical phenol ligand that does not saturate the coordination of the manganese ion. In the absence of an X-ray structure, the formulation of the compound was based on thorough characterization in the solid state and solution as well. Extensive studies of the phosphatase-like activity were reported similar to those for the compound obtained by Neves et al.[20]

In order to investigate the electronic properties of biologically relevant iron−manganese complexes and ultimately their reactivity, we prepared such complexes of the unsymmetrical ligand HL-Bn {[2-bis[(2-pyridylmethyl)-aminomethyl]]-6-[benzyl-2-(pyridylmethyl)aminomethyl]-4-methylphenol;[23] Scheme 1}. As shown for the diiron[24,25] and dimanganese[26] analogues, this ligand does not saturate the coordination of one metal ion that binds an exchangeable solvent molecule (e.g., H_2O, CH_3OH), thus allowing the complexes to efficiently activate peroxides.[27,28] In this Article, we report the synthesis and characterization of the $Fe^{III}Mn^{II}$, $[Fe^{III}Mn^{II}(L\text{-}Bn)(OAc)_2(OH_2)](ClO_4)_2$ (**1**), and $Fe^{II}Mn^{II}$, $[Fe^{II}Mn^{II}(L\text{-}Bn)(OAc)_2(OH_2)](ClO_4)$ (**2**), complexes of this ligand, together with a thorough investigation of their spectroscopic properties. Extensive studies of the phosphatase-like activity of **1** including a comparison with its homodinuclear analogues will be reported in a separate article.

Scheme 1. Ligand HL-Bn

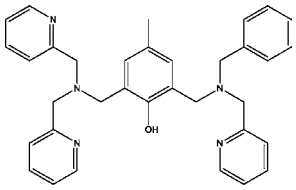

EXPERIMENTAL SECTION

All solvents and reagents were of the highest quality available and were used as received unless noted otherwise. The ligand HL-Bn was prepared as described previously.[23]

Syntheses. *$[Fe^{III}Mn^{II}(L\text{-}Bn)(OAc)_2(OH_2)](ClO_4)_2$ (1).* Complex **1** was synthesized according to the following procedure. A solution of 0.165 g (0.31 mmol) of HL-Bn and 0.050 g (0.62 mmol) of sodium acetate in 50 mL of methanol (MeOH) was treated with a solution of 0.160 g (0.31 mmol) of $Fe(ClO_4)_3{\cdot}9H_2O$ and 0.113 g (0.31 mmol) of $Mn(ClO_4)_2{\cdot}6H_2O$ in 5 mL of MeOH. After stirring for 1 h, the mixture was left overnight. The purple precipitate that formed was filtered and washed with MeOH. Recrystallization from MeOH/water (H_2O) (90:10) afforded dark-blue crystals that were of diffraction quality (yield: 65%). Anal. Calcd for $\mathbf{1}{\cdot}H_2O$, $C_{38}H_{44}Cl_2Fe_1Mn_1N_5O_{15}$: C, 45.99; H, 4.47; N, 7.06; Cl, 7.14. Found: C, 45.59; H, 4.30; N, 7.28; Cl, 7.18. ESI-MS (positive ion in CH_3CN): m/z 378.6 (100%) ($[\mathbf{1} - H_2O - 2ClO_4]^{2+}$), 856.1 (10%) ($[\mathbf{1} - H_2O - ClO_4]^{+}$).

$[Fe^{II}Mn^{II}(L\text{-}Bn)(OAc)_2(OH_2)](ClO_4)$ (2). Complex **2** was synthesized by a similar procedure. To a solution of 0.200 g (0.38 mmol) of HL-Bn in 3 mL of MeOH was added 0.137 g (0.38 mmol) of $Fe(ClO_4)_2{\cdot}6H_2O$ in a MeOH solution followed by 0.137 g (0.38 mmol) of $Mn(ClO_4)_2{\cdot}6H_2O$ and 0.062 g (0.76 mmol) of sodium acetate under anaerobic conditions. The solution was allowed to stir overnight. The yellow precipitate that formed was filtered and washed with MeOH (yield: 50%). Anal. Calcd for $\mathbf{2}{\cdot}H_2O$, $C_{38}H_{44}Cl_1Fe_1Mn_1N_5O_{11}$: C, 51.11; H, 4.97; N, 7.84. Found: C, 51.45; H, 4.94; N, 7.69. ESI-MS (positive ion in CH_3CN): m/z 757.3 (100%) ($[\mathbf{2} - H_2O - ClO_4]^{+}$).

Caution! *Perchlorate salts of metal complexes with organic ligands are potentially explosive.*

Spectroscopic Measurements. Electronic absorption spectra were recorded on a Perkin-Elmer Lambda 20 spectrophotometer. Electrospray ionization mass spectrometry (ESI-MS) spectra were obtained with a Thermo LXQ ESI source spectrometer with an ion trap and an octupolar analyzer. ^1H NMR spectra were recorded on a Bruker AC 200 spectrometer. The sample oxidation was prevented by inclusion of the sample in an NMR tube fitted with a Young valve.

X-ray Structural Analysis. The data sets for the single-crystal X-ray studies were collected with Mo Kα radiation on a Bruker SMART three-circle diffractometer using *SMART* and *SAINT* software for data collection and data reduction.[29] All calculations were performed using the *SHELXTL* program.[30] The structure was solved by direct methods and refined by full-matrix least squares on F^2. Complete information on the crystal data and data collection parameters is given in the Supporting Information, with a summary in Table 1.

Table 1. Summary of Crystallographic Data for Complex 1

formula	$C_{38}H_{44}Cl_2FeMnN_5O_{15}$
fw	992.47
temperature/K	150(2)
wavelength λ(Mo Kα)/Å	0.71073
cryst syst	monoclinic
space group	$P2_1/c$
a/Å	21.2114(10)
b/Å	10.9132(11)
c/Å	20.5111(10)
β/deg	116.631(6)
V/Å^3	4244.3(5)
Z	4
D_c/g·cm^{-3}	1.553
μ/mm^{-1}	0.840
F(000)	2048
abs corrn	semiempirical from equivalents
transmn factors (T_{max} and T_{min})	0.9513 and 0.7298
reflns	7900
param/restraints	641/13
GOF (F^2)	1.036
$R(F)$ [$I > 2\sigma(I)$]	0.0495
$Rw(F^2)$ (all data)	0.1205

Electrochemistry. Electrochemical measurements were carried out using a PAR model 273 potentiostat. All electrochemical experiments were run under an argon atmosphere in a glovebox, using a standard three-electrode electrochemical cell. All potentials were referred to a Ag/AgCl(saturated) reference electrode in an acetonitrile/0.1 M tetra-*n*-butylammonium perchlorate (TBAP) electrolyte. The potential of the regular ferrocene/ferrocenium (Fc/Fc^+) redox couple used as an internal standard was 0.36 V under our experimental conditions. The working electrodes were platinum disks polished with 1 μm diamond paste that were 5 mm in diameter for cyclic voltammetry (E_{pa}, anodic peak potential; E_{pc}, cathodic peak potential; $E_{1/2} = (E_{pa} + E_{pc})/2$; ΔE_p

$= E_{pa} - E_{pc}$) and 2 mm in diameter for rotating-disk-electrode experiments.

Magnetic Measurements. The magnetic susceptibility of compounds **1** and **2** was measured on a MPMS Quantum Design magnetometer operating over the temperature range 2−300 K at 5 and 30 kOe. The samples (35.31 and 9.71 mg for **1** and **2**, respectively) were contained in an aluminum bucket that had been independently calibrated. Only data superimposable at the two recording fields were considered for analysis. They were corrected from diamagnetism using Pascal's constants[31] and were simulated using the van Vleck equation derived from the Heisenberg exchange Hamiltonian ($\hat{H} = J\hat{S}_1\cdot\hat{S}_2$).[31]

Electron Paramagnetic Resonance (EPR) Spectroscopy. EPR spectra were recorded on an X-band Bruker EMX spectrometer equipped with an Oxford Instruments ESR-900 continuous-flow helium cryostat and an ER-4116 DM Bruker cavity. Q-band EPR spectra were recorded with a Bruker EMX, equipped with the ER-5106 QTW Bruker cavity and an Oxford Instruments ESR-900 continuous-flow helium cryostat. All spectra presented were recorded under nonsaturating conditions.

Theoretical Calculation of EPR spectra. The EPR spectrum of **2** was calculated assuming a $S_{eff} = {}^1/_2$ system in interaction with one manganese nuclear spin $I_{Mn} = {}^5/_2$. The electronic Zeeman and manganese hyperfine interactions were parametrized by collinear matrices. The energy of the transitions was calculated by treating the hyperfine interaction as a second-order perturbation of the Zeeman effect.[32] The transitions were convoluted assuming the well-known angular variation of the g values with a line-width parameter given in energy units.[33] Theoretical spectra for dinuclear complexes were calculated using the XSophe Computer Simulation Software Suite (*XSophe*, version 1.1.4) developed by the department of Mathematics at the University of Queensland, Brisbane, Australia, and obtained from Bruker Analytik GmbH, Rheinstetten, Germany. Calculations were performed by diagonalization of the energy matrices.

Mössbauer Spectroscopy. ^{57}Fe Mössbauer experiments were performed using a 50 mCi source of ^{57}Co(Rh). Spectra were recorded at 4.2 K on a low-field Mössbauer spectrometer equipped with a Janis SVT-400 cryostat or at variable temperatures (1.4−80 K) using a strong-field Mössbauer spectrometer equipped with an Oxford Instruments Spectromag 4000 cryostat containing an 8 T split-pair superconducting magnet. The 14.4 keV γ-rays were detected by means of a proportional counter, and Mössbauer spectra were recorded on a 512 multichannel analyzer working in the multiscaling mode. The system was calibrated with a metallic iron absorber at room temperature, and all velocity scales and isomer shifts are referred to the iron standard. The temperature of the sample was measured with a platinum resistor. A conventional liquid-helium, horizontal transmission cryostat was used; the source was maintained at room temperature and moved by a constant-acceleration electromechanical drive system under feedback control.

Simulation of Mössbauer and EPR Spectra. Mössbauer spectra of complex **1** were fitted as described using a homemade program. It was implemented to allow the *simultaneous* minimization of Mössbauer and X-band EPR spectra of complex **2**. The minimization procedure relied on a genetic algorithm.[34] Calculation of the nuclear transitions of the Mössbauer spectra was performed in the electric-field-gradient (EFG) frame of the iron site. Electronic tensors and matrices are expressed in the zero-field-splitting (ZFS) frame of the iron site. The ZFS frame was rotated with respect to the Fe EFG one. The three successive Euler rotations defined as follows allowed one to bring the EFG frame (x_0, y_0, z_0) in coincidence with the ZFS tensor principal axes (x_3, y_3, z_3): (i) rotation through an angle χ about the z_0 axis generating the (x_1, y_1, z_1) frame; (ii) rotation through an angle ρ about the y_1 axis generating the (x_2, y_2, z_2) frame; (iii) rotation through an angle τ about the z_2 axis generating the (x_3, y_3, z_3) frame. The powder X-band EPR spectrum was calculated by relying on the dinuclear structure of complex **2**, with EPR transitions originating only from the lowest Kramers doublet. These two levels were assumed to behave linearly upon the applied magnetic field and to present a constant electronic composition between 200 and 700 mT. The validity of these hypotheses was verified a posteriori. The manganese hyperfine interaction ($I_{Mn} = {}^5/_2$, 100% natural abundance) was calculated as a second-order perturbation of the electronic Zeeman interaction within the ground-state doublet. Perturbations due to the excited-state Kramers doublets are thus excluded. Consequently, for each orientation of the applied magnetic field, the magnitude B corresponding to the transition between the manganese nuclear level $|v_{-,i}\rangle$ ($i = 1-6$) of the lower electronic level and the manganese nuclear level $|v_{+,j}\rangle$ ($j = 1-6$) of the upper electronic level (see Scheme 2) is the root of eq 1.

Scheme 2. Removal of the Degeneracy of the Ground-State Kramers Doublet of Complex 2 upon Application of an External Magnetic Field[a]

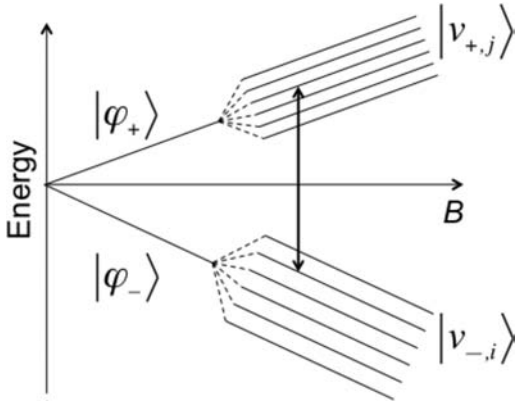

[a]The left part of the diagram shows the two electronic Zeeman levels labeled $|\varphi_+\rangle$ and $|\varphi_-\rangle$. The difference between the slopes of the upper and lower levels is equal to $e_+^{(0)} - e_-^{(0)}$. The right part of the diagram shows the first-order manganese hyperfine splittings that differ for the two electronic Zeeman levels. The arrow represents one of the 36 possible EPR transitions between one out of the six lower manganese nuclear levels $|v_{-,i}\rangle$ ($i = 1-6$) and one out of the six upper manganese nuclear levels $|v_{+,j}\rangle$ ($j = 1-6$).

$$[e_+^{(0)} - e_-^{(0)}]B + [e_{+,j}^{(1)} - e_{-,i}^{(1)}] + \frac{[e_{+,j}^{(2)} - e_{-,i}^{(2)}]}{[e_+^{(0)} - e_-^{(0)}]B} - h\nu = 0 \quad (1)$$

where the four terms from left to right stand for the electronic Zeeman interaction, the first- and second-order corrections of the manganese hyperfine interaction, and the energy quantum of the EPR transition, respectively.

The $e_\pm^{(0)}$ and $e_{\pm,k}^{(n)}$ quantities ($n = 1-2$ and $k = 1-6$) were determined at 0.4 T. The $e_\pm^{(0)}$ terms were calculated by exact diagonalization of the energy matrix of the $Fe^{II}Mn^{II}$ complex that included the iron ZFS, the iron and manganese Zeeman effects, and the isotropic exchange interaction. The diagonalization procedure also leads to the two eigenvectors $|\varphi_\pm\rangle$ of the lowest Kramers doublet, which are expressed as a linear combination of the $|m_{Mn}, m_{Fe}\rangle$ basis functions, where m_{Mn} and m_{Fe} are the electronic manganese and iron spin projections along the principal z direction of the iron ZFS interaction, respectively. It must be noted that, because of the competitive iron ZFS and exchange interactions in complex **2**, the linear combinations for $|\varphi_+\rangle$ and $|\varphi_-\rangle$ are different. Once the electronic compositions of the lowest Kramers doublet are known, the two 6×6 manganese hyperfine matrices with elements $\langle\varphi_+,M_q|\hat{S}_{Mn}\tilde{a}_{Mn}\hat{I}_{Mn}|\varphi_+,M_p\rangle$ and $\langle\varphi_-,M_q|\hat{S}_{Mn}\tilde{a}_{Mn}\hat{I}_{Mn}|\varphi_-,M_p\rangle$ ($p, q = 1-6$), where M_p and M_q are the manganese nuclear-spin projections and run from $-{}^5/_2$ to $+{}^5/_2$ by unit step, are determined. The $e_{+,j}^{(1)}$ and $e_{-,i}^{(1)}$ terms ($i, j = 1-6$) correspond to the eigenvalues obtained by diagonalization of these two 6×6 blocks. The associated eigenvectors labeled $|v_{+,j}\rangle$ and $|v_{-,i}\rangle$ ($i, j = 1-6$) are linear combinations of the functions $|\varphi_+,M_q\rangle$ and $|\varphi_-,M_p\rangle$ ($p, q = 1-6$), respectively. The

dx.doi.org/10.1021/ic301725z | Inorg. Chem. 2012, 51, 10447−10460

difference between $|\varphi_+\rangle$ and $|\varphi_-\rangle$ leads to different first-order corrections and different linear combinations for $|v_{+,j}\rangle$ and $|v_{-,i}\rangle$ (i, j = 1−6) (see Scheme 2). The second-order terms depend on the off-diagonal elements $\langle v_{+,j}|\hat{S}_{Mn}\tilde{a}_{Mn}\hat{I}_{Mn}|v_{-,i}\rangle$ (i, j = 1−6). The $e^{(2)}_{-,i}$ terms (i = 1−6) (respectively $e^{(2)}_{+,j}$, j = 1−6) associated with the second-order corrections for the lower (respectively upper) Zeeman level are given by eq 2a (respectively eq 2b).

$$e^{(2)}_{-,i} = -\sum_{l=1}^{6} |\langle v_{+,l}|\hat{S}_{Mn}\tilde{a}_{Mn}\hat{I}_{Mn}|v_{-,i}\rangle|^2 \quad (2a)$$

$$e^{(2)}_{+,j} = +\sum_{k=1}^{6} |\langle v_{+,j}|\hat{S}_{Mn}\tilde{a}_{Mn}\hat{I}_{Mn}|v_{-,k}\rangle|^2 \quad (2b)$$

The probability associated with the transition between the manganese nuclear levels $|v_{-,i}\rangle$ (i = 1−6) on the one side and $|v_{+,j}\rangle$ (j = 1−6) on the other is the product of the nuclear overlap term associated with $|\langle v_{+,j}|v_{-,i}\rangle|^2$ and the common electronic Zeeman term given by eq 3:

$$|\langle\varphi_+|\mu_B\hat{B}_1\tilde{g}_{Fe}\hat{S}_{Fe} + \mu_B\hat{B}_1\tilde{g}_{Mn}\hat{S}_{Mn}|\varphi_-\rangle|^2 \quad (3)$$

where B_1 stands for the magnetic field associated with the microwave that is perpendicular to the external magnetic field B.

Because the $e^{(0)}_{\pm}$ quantities are independent of B for a given orientation of the magnetic field, the electronic component of the transition probability can be equivalently calculated according to eq 4:

$$\frac{1}{g^2}\{g_x^2 g_y^2 \sin^2\theta + g_y^2 g_z^2(\sin^2\varphi + \cos^2\theta\cos^2\varphi) + g_x^2 g_z^2(\cos^2\phi + \cos^2\theta\sin^2\phi)\} \quad (4)$$

where θ and φ refer to the orientation of the magnetic field (spherical coordinates). g is related to the g_k factors ($k = x, y, z$) according to the usual relationship $g^2 = g_x^2\sin^2\theta\cos^2\varphi + g_y^2\sin^2\theta\sin^2\varphi + g_z^2\cos^2\theta$. The g_k factors ($k = x, y, z$) are obtained from the $e^{(0)}_{\pm}$ terms calculated at 0.4 T when the magnetic field is along the x, y, and z directions according to eq 5.

$$g_k = \frac{[e^{(0)}_+ - e^{(0)}_-]B}{\mu_B B} \quad (5)$$

They are indeed the average effective g factors associated with the lowest Kramers doublet when small external magnetic fields are applied.

As previously, the transitions were convoluted, assuming the angular variation of the g values with a line-width parameter given in energy units.[33]

RESULTS

Synthesis of 1 and 2. *Synthesis of 1.* Previous studies have shown that the diiron[24] and dimanganese[26] analogues of **1** can be readily prepared by mixing the ligand and iron or manganese salts. Therefore, the addition of 1 equiv of each salt to the ligand could, in principle, produce a statistical mixture of diiron, iron−manganese, and dimanganese complexes. However, crystallographic analyses of the homodinuclear mixed-valent $Fe^{III}Fe^{II}$[24] and $Mn^{III}Mn^{II}$[26] complexes reveal that the M^{III} ion always binds to the bis(picolylamine) site (hereafter refered to as A in $^{A}M/^{B}M'$). We thus reasoned that the treatment of the ligand with 1 equiv each of ferric and manganous perchlorates in the presence of sodium acetate should give the desired $Fe^{III}Mn^{II}$ compound. Figure 1 shows that the positive-mode ESI-MS spectrum of complex **1** presents a major peak at m/z 378.6 that corresponds to the dication $[Fe^{III}Mn^{II}(L\text{-}Bn)(OAc)_2]^{2+}$ and a second peak at m/z 856.1 associated with the monocation $\{[Fe^{III}Mn^{II}(L\text{-}Bn)(OAc)_2](ClO_4)\}^+$. As shown in Figure 1, the experimental mass profile of **1** matches

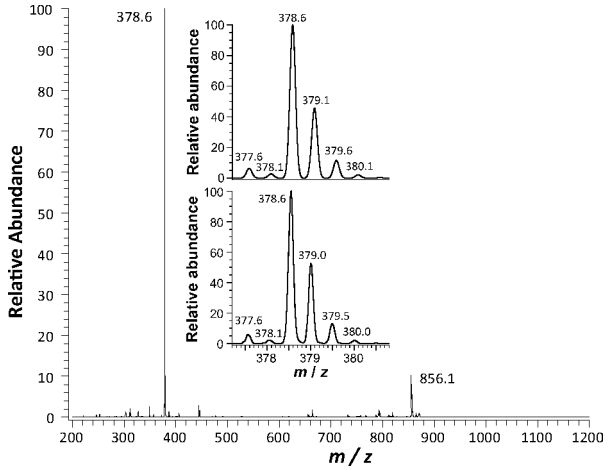

Figure 1. Positive-mode ESI-MS spectrum of complex **1**. The inset reproduces a zoom of the m/z 378.6 pattern (bottom, experimental spectrum; top, calculated spectrum).

perfectly the theoretical one for the iron−manganese complex. The quality of this match is of particular significance for the peaks at m/z 378.1 and 379.1 corresponding to the dimanganese and diiron species, respectively, because it shows that **1** is not contaminated to a significant extent by the latter species. The presence of the ferric ion will be evidenced by Mössbauer spectroscopy, and the respective locations of the two ions will be confirmed by the X-ray crystallographic determination of **1** and Mössbauer spectroscopy.

Synthesis of 2. The synthesis of **2** proved more difficult than that of **1** because of the identical charges of the two cations. Indeed, the directing effect provided in **1** by the preference of the bis(picolylamine) site for the ferric site was lacking, leading to the potential formation of the homodinuclear diiron and dimanganese complexes as well as the two position isomers $^{A}Fe/^{B}Mn$ and $^{A}Mn/^{B}Fe$. The formation of the pure $^{A}Fe/^{B}Mn$ complex could be achieved by successive additions of 1 equiv of carefully titrated solutions of iron salt and then of manganese salt. Alternatively, as shown below (inset in Figure 3), **2** can be obtained by stoichiometric cobaltocene reduction of **1**. The latter procedure afforded **2** with less contamination if any. The positive-mode ESI-MS spectrum of **2** shown in Figure S1 in the Supporting Information (SI) presents a single intense peak at m/z 757.2, in agreement with the formulation of **2** as a iron−manganese complex. This is supported by the near-perfect match of the experimental and theoretical isotopic patterns, which further indicates the absence of significant contamination by the homodinuclear analogues.

X-ray Structure of 1. Recrystallization of **1** in a 9:1 $MeOH/H_2O$ mixture afforded well-formed purple crystals that were suitable for single-crystal X-ray analysis. The structure of the cation is illustrated in Figure 2. The crystal parameters are listed in Table 1, and important bond distances and angles are summarized in Table 2. The crystal structure confirms the heterodinuclear nature of **1** and allows the two metal sites to be assigned (see below). The two metal ions are hexacoordinated. They are bridged by the phenolate oxygen atom and the carboxylate groups of two μ-1,3-acetates. The coordination of one metal is complemented by the three nitrogen atoms of a bis(picolyl)amine branch and that of the other metal by two nitrogen atoms from a picolylamine and one oxygen atom from

dx.doi.org/10.1021/ic301725z | Inorg. Chem. 2012, 51, 10447−10460

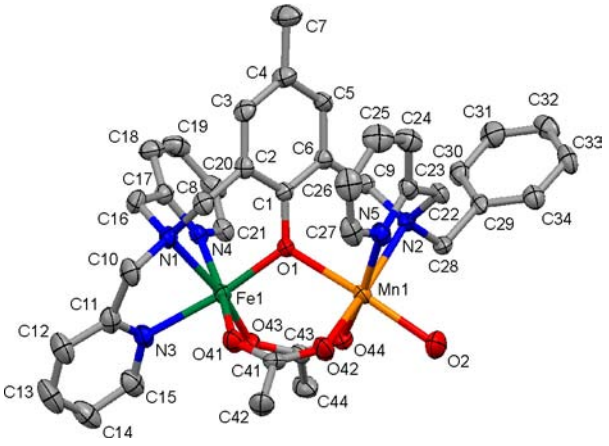

Figure 2. ORTEP diagram of the cation of **1** displaying the atom-labeling scheme. 50% probability thermal ellipsoids are depicted. Hydrogen atoms have been omitted for clarity.

Table 2. Important Bond Lengths (Å) and Angles (deg) for Complex 1

Fe1–O1	1.937(2)	Mn1–O42	2.112(3)
Fe1–O43	1.951(2)	Mn1–O44	2.138(2)
Fe1–O41	1.972(2)	Mn1–O2	2.162(3)
Fe1–N4	2.159(3)	Mn1–O1	2.188(2)
Fe1–N3	2.150(3)	Mn1–N5	2.241(3)
Fe1–N1	2.186(3)	Mn1–N2	2.322(3)
Fe1–O1–Mn1	113.73(10)		
O1–Fe1–O43	100.88(9)	O42–Mn1–O44	96.82(10)
O1–Fe1–O41	94.82(9)	O42–Mn1–O2	90.14(11)
O43–Fe1–O41	99.60(10)	O44–Mn1–O2	85.41(12)
O1–Fe1–N4	86.97(9)	O42–Mn1–O1	91.92(9)
O43–Fe1–N4	89.85(10)	O44–Mn1–O1	87.17(8)
O41–Fe1–N4	169.85(10)	O2–Mn1–O1	172.48(11)
O1–Fe1–N3	166.51(10)	O42–Mn1–N5	91.40(11)
O43–Fe1–N3	92.31(10)	O44–Mn1–N5	169.70(10)
O41–Fe1–N3	80.05(10)	O2–Mn1–N5	100.82(12)
N4–Fe1–N3	95.98(10)	O1–Mn1–N5	86.36(9)
O1–Fe1–N1	91.53(10)	O42–Mn1–N2	167.47(10)
O43–Fe1–N1	162.06(9)	O44–Mn1–N2	95.48(10)
O41–Fe1–N1	92.13(10)	O2–Mn1–N2	93.23(11)
N4–Fe1–N1	77.82(11)	O1–Mn1–N2	86.28(8)
N3–Fe1–N1	76.30(11)	N5–Mn1–N2	76.11(10)

an exogeneous H_2O molecule. Average metal distances around the two metal atoms amount to 2.059 Å for the metal bound to the bis(picolyl)amine branch and to 2.194 Å for that bound to the H_2O molecule, which allows one to conclude that the M^{III} ion is bound to the bis(picolyl)amine branch and the M^{II} ion to the H_2O molecule. However, as observed earlier,[18] because of the similar sizes of the ions, the structure cannot discriminate between iron and manganese. Nevertheless, Mössbauer spectroscopy identifies a ferric center in **1** (see below). Therefore, it appears that the coordination of the Fe^{III} ion (Fe1) is complemented by the three nitrogen atoms of the bis(picolyl)-amine branch, whereas the coordination of the Mn^{II} ion (Mn1) is completed by two nitrogen atoms, N2 and N5, and O2 from a H_2O molecule. This $^{A}Fe^{III}/^{B}Mn^{II}$ assignment is consistent with previous crystallographic data that revealed the preference of the M^{III} ion for the bis(picolylamine) branch.[24−26] Moreover, a close examination of Table 3, which compares

Table 3. Comparison of the Bond Distances (Å) of 1 and Homodinuclear Complexes[24,26a]

	Mn–Mn	Fe–Mn	Fe–Fe
M_1–O(phen)	1.873(2)	1.937(2)	1.952(4)
M_1–O(carb-trans)	1.961(2)	1.951(2)	1.948(5)
M_1–O(carb-cis)	2.057(2)	1.972(2)	1.996(5)
M_1–N(tert)	2.130(2)	2.186(3)	2.215(5)
M_1–N(py-cis)	2.221(2)	2.159(3)	2.173(7)
M_1–N(py-trans)	2.050(2)	2.150(3)	2.156(8)
average M_1–L	2.049	2.059	2.073
M_2–O(phen)	2.245(2)	2.188(2)	2.115(6)
M_2–O(carb-trans)	2.096(2)	2.112(3)	2.084(6)
M_2–O(carb-cis)	2.130(2)	2.138(2)	2.128(6)
M_2–N(tert)	2.353(2)	2.322(3)	2.254(5)
M_2–N(py-cis)	2.237(2)	2.241(3)	2.191(7)
M_2–O(lig)	2.143(2)	2.162(3)	2.156(8)
average M_2–L	2.201	2.194	2.155

[a]For all complexes, labeled M_1M_2, the exogeneous ligand (H_2O or MeOH), denoted as O(lig), is bound to metal site 2. The metal ligands are designated as follows: O(phen) = bridging phenolate; N(tert) = tertiary nitrogen; N(py-trans) = pyridine nitrogen trans to the phenolate; N(py-cis) = pyridine nitrogen cis to the phenolate; O(carb-trans) = carboxylate oxygen trans to the tertiary N; O(carb-cis) = carboxylate oxygen cis to the tertiary nitrogen.

the bond distances of **1** with those of the $^{A}Fe^{III}/^{B}Fe^{II}$ and $^{A}Mn^{III}/^{B}Mn^{II}$ analogues, illustrates the closer similarity of the metal environments of **1** with those of Fe^{III}[24] and Mn^{II}[26] in the homodinuclear analogues.

Electronic Absorption Spectroscopy. The electronic absorption spectrum of **1** in acetonitrile (solid line in Figure 3)

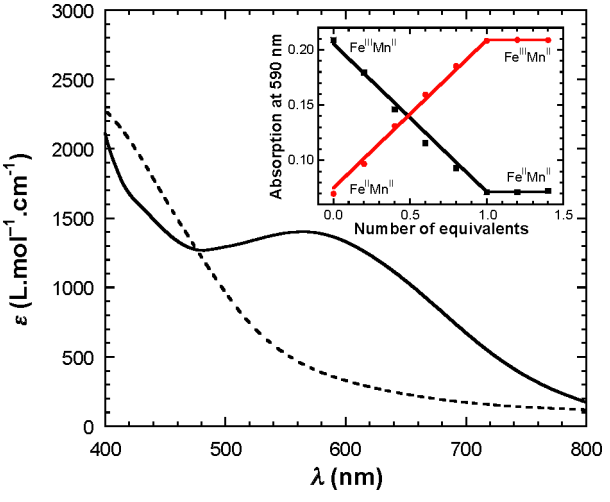

Figure 3. Electronic absorption spectra of complexes **1** (solid line) and **2** (dashed line). The inset shows the titration of a 0.18 mM solution in MeOH of compound **1** by cobaltocene (black squares) and of compound **2** by cerium ammonium nitrate (red dots).

consists of a broad band centered at 568 nm (ε = 1400 $L{\cdot}mol^{-1}{\cdot}cm^{-1}$). The energy and intensity of this band are similar to those observed (λ_{max} = 578 nm; ε = 1300 $L{\cdot}mol^{-1}{\cdot}cm^{-1}$) for the mixed-valent $[Fe^{III}Fe^{II}(L\text{-}Bn)(mpdp)(CH_3CN)](ClO_4)_2$,[25] which is assigned to the metal–ligand charge transfer $p\pi \rightarrow d\pi^*$ from the bridging phenolate ligand to the Fe^{III} ion.[23] Therefore, the phenolate-to-Fe^{III} charge-transfer transition is not significantly affected by the M^{II} ion. No

dx.doi.org/10.1021/ic301725z | Inorg. Chem. 2012, 51, 10447−10460

intervalence charge-transfer band can be observed in the near-IR region for complex **1**. As expected, because of the Fe^{II} and Mn^{II} compositions, no specific absorption is detected in the visible domain for complex **2** (dashed line in Figure 3).

Redox Properties. The electrochemical properties of **1** have been investigated in acetonitrile/0.1 M TBAP at a platinum electrode. As shown in Figure 4, **1** exhibits a

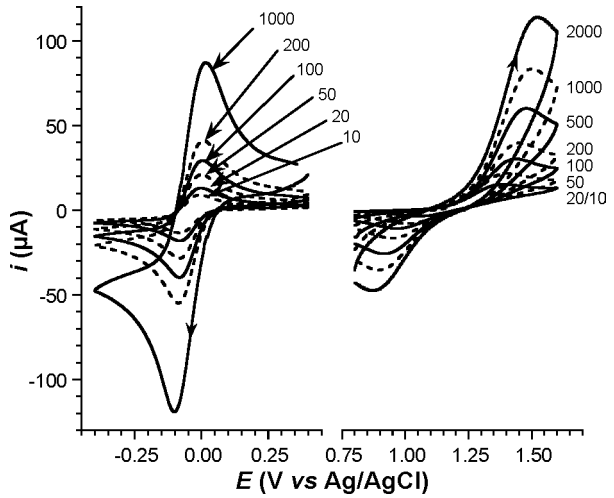

Figure 4. Cyclic voltammograms of **1** (1.1 mM) at a platinum electrode (diameter: 5 mm) in acetonitrile/0.1 M TBAP at various sweep rates (indicated in $mV \cdot s^{-1}$).

quasireversible reduction at $E_{1/2} = -0.040$ V vs Ag/AgCl (ΔE_p = 87 mV) corresponding to the $Fe^{III}Mn^{II}/Fe^{II}Mn^{II}$ redox couple. This potential is independent of the sweep rate in the range 10−1000 $mV \cdot s^{-1}$. On the other hand, in the same conditions (ν = 100 $mV \cdot s^{-1}$), **1** presents an oxidation peak at 1.45 V vs Ag/AgCl, with an associated reduction peak at 0.97 V pointing to an electrochemically irreversible behavior. Repeated cycling over the potential range from 0.8 to 1.6 V vs Ag/AgCl did not evidence any intensity change in the peaks, suggesting that the oxidation−reduction cycle is chemically reversible. A systematic study of the sweep rate dependence of the potentials of these peaks revealed that their separation increased with the sweep rate from 320 mV at 10 $mV \cdot s^{-1}$ to 650 mV at 2 $V \cdot s^{-1}$. Overall, these results indicate that the $Fe^{III}Mn^{II}/Fe^{III}Mn^{III}$ couple involves a slow heterogeneous electron transfer. A similar behavior was observed for the one-electron oxidation of mononuclear Mn(II) bis-terpyridine complexes.[35−38] Different hypotheses have been advanced to explain it: (i) poor contact between the complex and electrode, (ii) poisoning of the electrode by adsorption of the oxidized species, and (iii) a structural change associated with oxidation of the isotropic Mn^{II} to the Jahn−Teller distorted Mn^{III}. The quasireversibility of the reductive transfer observed for **1** does not support the first hypothesis. Furthermore, the electrochemical studies of the homodinuclear complexes[25,26] have never shown any adsorption process, thereby making the second hypothesis less likely. Distortion of the metal coordination linked to the electron transfer appears therefore the most likely explanation of this irreversible behavior. A similar electrochemical irreversibility was observed for the $Fe^{III}Mn^{II}/Fe^{III}Mn^{III}$ couple in the complex reported by Neves et al.[20]

Interestingly, the potential of the $Fe^{III}Mn^{II}/Fe^{II}Mn^{II}$ couple occurs within 30 mV of that of the $Fe^{III}Fe^{II}/Fe^{II}Fe^{II}$ couple. This observation supports again the localization of the iron ion in the bis(picolylamine) site. Because the same observation was made by Buchanan et al.[15] and Neves et al.,[20] it appears to be a general feature of this kind of compound. Overall, it shows that the reduction of the ferric ion in this site is not very sensitive to the nature of the metal (Mn^{II} vs Fe^{II}) in the other site. A detailed study of the homodinuclear complexes has shown that the electrochemical properties of this kind of complex is far more dependent on Coulombic interactions than on electronic delocalization or exchange interaction between the metal centers.[23] If this were true also for the iron−manganese complex, one can predict that **1** would have a stability domain of the mixed-valent species of ca. 800 mV, a value intermediate between those of the homodinuclear analogues (Mn_2, 730 mV; Fe_2, 880 mV), and therefore an oxidation potential ca. 0.76 V, far below the observed potential for the oxidation of **1**. This illustrates that the redox properties of the Mn^{II} site are strongly dependent on the nature of the vicinal metal, Mn^{III} vs Fe^{III}. Because the Jahn−Teller effect provides a reasonable explanation of the observed slow electron transfer, it can tentatively explain also why **1** differs from the $Mn^{III}Mn^{II}$ homologue, which exhibited a quasireversible oxidation to the $Mn^{III}Mn^{III}$ state.[26] Indeed, it may be tentatively argued that in the latter complex the second metal Mn^{III} is more prone to distortion and thus has a larger plasticity than Fe^{III}, which is more rigid, and might then hinder the rearrangement of the coordination sphere of its neighbor by blocking a face of its coordination octahedron. This hindrance would disfavor the oxidation of the manganese site and increase the stability domain of the mixed-valent species.

The inset in Figure 3 illustrates the reaction of **1** in MeOH with cobaltocene monitored by the evolution of the absorbance at 590 nm. This shows that the absorbance of the charge-transfer transition is bleached after the addition of 1 equiv of cobaltocene, as expected for the reduction of Fe^{III} to Fe^{II}. This reaction was successfully used as an alternate procedure to prepare **2**. Interestingly, as shown in Figure 3, **1** can be quantitatively regenerated by the oxidation of **2** by a stoichiometric amount of cerium ammonium nitrate.

Magnetic Properties of Compound 1. *Magnetic Susceptibility.* The $\chi_M T$ vs T curve for a powder sample of compound **1** is reproduced in Figure 5. At 300 K, the $\chi_M T$ value is 6.35 $cm^3 \cdot K \cdot mol^{-1}$. This value is significantly below 8.75 $cm^3 \cdot K \cdot mol^{-1}$, the value expected for two noninteracting high-spin Fe^{III} ($S_{Fe} = {}^5/_2$) and Mn^{II} ($S_{Mn} = {}^5/_2$) ions. This suggests an antiferromagnetic interaction between the two ions. This conclusion is confirmed by the continuous decrease of the $\chi_M T$ product upon a decrease in the temperature. $\chi_M T$ reaches a zero plateau below 8 K, indicating an $S = 0$ ground state for **1**. The data were fitted according to the well-known van Vleck formula for two interacting ${}^5/_2$ spins. The best fit was obtained with J = 20(1) cm^{-1} ($\hat{H} = J\hat{S}_{Fe} \cdot \hat{S}_{Mn}$). The g factor was fixed to 2.0 because of the local half-filled 3d shells. The obtained J value is close to those of previously published μ-phenoxobis(μ-acetato)iron(III)manganese(II) systems: 13.6 cm^{-1} in [FeMn(bpbpmp)(μ-OAc)$_2$](ClO$_4$),[20] 15.4 cm^{-1} in [FeMn(bimp)(μ-OAc)$_2$](ClO$_4$)$_2$,[15] 19.2 cm^{-1} in [FeMn(ipcpmp)(μ-OAc)$_2$(CH$_3$OH)](PF$_6$)[22] and 23 cm^{-1} in [FeMn(bpmp)(μ-OAc)$_2$](BPh$_4$)$_2$[18] {H$_2$bpbpmp = 2-[bis(2-pyridylmethyl)-aminomethyl]-6-[2-(hydroxybenzyl)(2-pyridylmethyl)-aminomethyl]-4-methylphenol, Hbimp = 2,6-bis[bis[(1-methylimidazol-2-yl)methyl]aminomethyl]-4-methylphenol, H$_2$ipcpmp = 2-[*N*-isopropyl-*N*-(2-pyridylmethyl)-

dx.doi.org/10.1021/ic301725z | *Inorg. Chem.* 2012, 51, 10447−10460

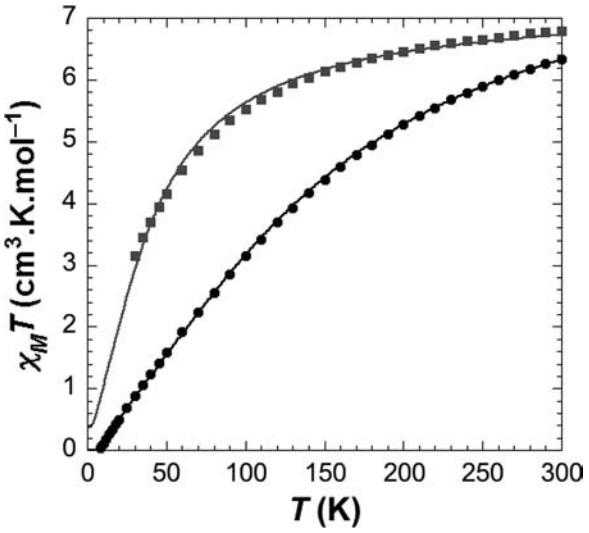

Figure 5. Experimental (full circles and squares) and theoretical (solid lines) $\chi_M T$ vs T curve measured on powder samples of compounds **1** (black) and **2** (gray). The theoretical trace is obtained with J = 20.4 cm^{-1} (g = 2.0 fixed) for **1** and with g = 1.99 and J = 6.8 cm^{-1} for **2**.

aminomethyl]-6-[*N*-(carboxylmethyl)-*N*-(2-pyridylmethyl)-aminomethyl]-4-methylphenol, and Hbpmp = 2,6-bis[bis(2-pyridylmethyl)aminomethyl]-4-methylphenol}.

Mössbauer Spectroscopy. To further characterize compound **1**, Mössbauer spectra were recorded on a solid-state sample at variable temperatures and external magnetic fields. The 4.2 K and 0 T spectrum corresponds to trace A in Figure 6. The signal is a single sharp quadrupole doublet, demonstrating that the iron ion occupies a single and well-defined binding site in **1**. The simulation of spectrum A gives δ = 0.46(1) mm·s^{-1}, $|\Delta E_Q|$ = 0.41(1) mm·s^{-1}, and Γ_{fwhm} = 0.28(1) mm·s^{-1}. These parameters are in agreement with a high-spin Fe^{III} site and are similar to the values measured for [FeMn(bpmp)(μ-$O_2CCH_2CH_3$)$_2$](BPh$_4$)$_2$ (δ = 0.45 mm·s^{-1} and ΔE_Q = 0.49 mm·s^{-1})[13] and [FeMn(bimp)(μ-OAc)$_2$](ClO$_4$)$_2$ (δ = 0.36 mm·s^{-1}; ΔE_Q = 0.65 mm·s^{-1}).[15] Spectra B and C in Figure 6 were recorded at 4.2 K under external magnetic fields of 4 and 7 T, respectively, applied perpendicularly to the γ beam. These spectra are well-reproduced assuming a single iron site with no spin density: δ = 0.46(2) mm·s^{-1}, ΔE_Q = −0.41(3) mm·s^{-1}, and Γ_{fwhm} = 0.28(5) mm·s^{-1}. These experiments thus confirm the S = 0 ground state of compound **1**. In addition, the negative sign of ΔE_Q was determined. The best simulations led to a rhombic Fe^{III} EFG tensor with η = 0.45, but values from 0 to 0.8 are equally satisfying. Only rhombicities close to 1 are precluded, indicating that the negative sign for the quadrupole splitting is meaningful. Mössbauer spectra were recorded between 4 and 80 K. Above 15 K, the spectra become broadened and lose resolution, indicating that the relaxation is neither in the slow relaxation limit nor in the fast one. Hence, only spectra recorded at 10.8 K were analyzed. They are reproduced in Figure 6 as traces D and E. From the magnetic susceptibility investigations, only the ground state of S = 0 and the first excited state of S = 1 are expected to be populated at this temperature with a ca. 85:15 distribution. However, the low population of the S = 1 level precludes detailed analysis. Simulations were thus performed assuming a dinuclear species with local electronic spins S_{Fe} = S_{Mn} = $^5/_2$ with no local ZFS effects and an intrinsic isotropic **g** matrix with g = 2.0. The

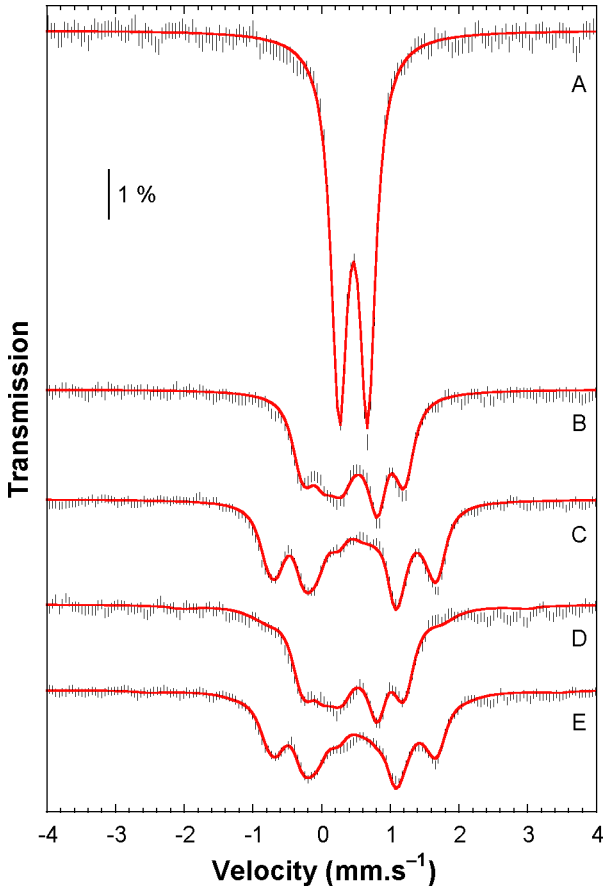

Figure 6. Experimental Mössbauer spectra (hatched marks) recorded on a 100% ^{57}Fe-enriched powder sample of complex **1** at 4.2 K (A−C) and 10.8 K (D and E). No external magnetic field was applied for spectrum A, while a magnetic field of 4 or 7 T was applied perpendicularly to the γ beam for traces B and D or C and E, respectively. Theoretical spectra are shown as solid lines. The 4.2 K spectra (A−C) are reproduced assuming a S = 0 ground state with the following parameters: δ = 0.46 mm·s^{-1}, ΔE_Q = −0.41 mm·s^{-1}, η = 0.45, and Γ_{fwhm} = 0.28 mm·s^{-1}. Identical theoretical traces are obtained assuming a dinuclear species with S_1 = S_2 = $^5/_2$ in the slow relaxation limit with the parameter set given as follows that allows one to reproduce spectra A−E: J = 19 cm^{-1}, δ = 0.46 mm·s^{-1}, ΔE_Q = −0.41 mm·s^{-1}, η = 0.45, a_{iso} = −23 T, and Γ_{fwhm} = 0.31 mm·s^{-1}.

nuclear parameters for the iron site were fixed to the values determined at 4.2 K. Only the exchange interaction between the Fe^{III} and Mn^{II} ions and the hyperfine interaction on the Fe^{III} site were varied. Furthermore, both interactions were taken as isotropic. Spectra D and E were satisfyingly reproduced in the slow relaxation limit with J = 19(4) cm^{-1} and a_{iso} = −23(2) T. The hyperfine coupling constant is consistent with a hexacoordinated high-spin ferric ion presenting a N/O coordination sphere.[39−42] In addition, the obtained J value is identical within experimental uncertainty with that determined from magnetic susceptibility measurements, validating the weak antiferromagnetic interaction between the two metal sites in **1**.

EPR Spectroscopy. A series of typical X- and Q-band spectra recorded on powder samples of compound **1** are reproduced in Figure 7. The 4.2 K X-band spectrum presents two signals. One is located at $g_{eff} \approx$ 4.3 and originates from mononuclear high-spin Fe^{II} or adventitious high-spin Fe^{II}. The second one is a six-line signal centered at g_{eff} = 2 and can be assigned to a

dx.doi.org/10.1021/ic301725z | *Inorg. Chem.* 2012, 51, 10447−10460

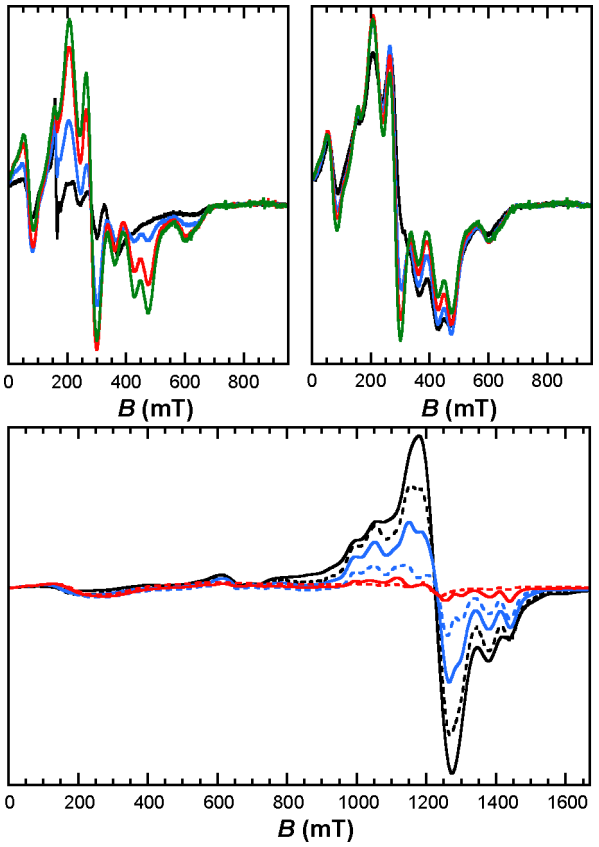

Figure 7. Experimental X-band (top panels, ν = 9.654 GHz) and Q-band (bottom panel, ν = 34 GHz) EPR spectra recorded on powder samples of complex **1**. Left top panel: T = 20 (black solid line), 30 (blue solid line), 45 (red solid line), and 55 K (green solid line). Right top panel: T = 55 (green solid line), 65 (red solid line), 80 (blue solid line), and 110 K (black solid line). Bottom panel: T = 15 (red dashed line), 28 (red solid line), 50 (blue dashed line), 81 (blue solid line), 102 (black dashed line), and 140 K (black solid line). Recording conditions: microwave power = 80 mW at X band and 4.6 mW at Q band; modulation frequency = 100 kHz; modulation amplitude = 0.5 mT.

mononuclear high-spin Mn^{II} species or adventitious high-spin Mn^{II}. The latter can be easily identified in the 15 K Q-band spectrum (see the zoom reproduced in Figure S2 in the SI). Upon an increase in the temperature, these two signals decrease in intensity, as expected for Curie law mononuclear species. Concomitantly, an increase in the temperature leads to the detection of new transitions. These are the signatures of the paramagnetic excited states of **1**.

Similar temperature-dependent EPR signatures have been previously reported in the literature for homodinuclear systems based on either Cr^{III},[43] Mn^{I},[44] Mn^{II},[45] or Fe^{III}[46,47] ions. Most of the published analyses were performed in the strong exchange limit, that is, when the ZFS of the metal ions are small compared to the exchange interaction. The EPR signal is thus a linear combination of the S-level signatures, with the weighted coefficients being directly proportional to the Boltzmann populations of a Zeeman level issued from the associated S state. The single electronic parameter controlling the weighted coefficients is the J constant.

Starting from 5 K and as the temperature is increased, the first state expected to contribute to the EPR signal is the S = 1 spin state. According to the exchange constant determined above [J = 20(1) cm^{-1}], one would expect its contribution to increase from 5 to 15−20 K, where a maximum is reached (see Figure S3 in the SI). No line in either the X- or Q-band series presents such a temperature behavior, indicating that this spin state is EPR-silent. This can be attributed to a strong ZFS effect. Indeed, it has been previously demonstrated that the S = 1 states of $[(edta)Fe^{III}(\mu\text{-}O)Fe^{III}(edta)]^{4-}$ and $[(phen)_2Fe^{III}(\mu\text{-}O)Fe^{III}(phen)_2]^{4+}$ complexes present no EPR transition even at the Q band due to the strong ZFS of the Fe^{III} site ($edta^{4-}$ = ethylenediaminetetraacetate; phen = 1,10-phenanthroline).[46] This hypothesis can still hold in the present case in spite of the presence of a single Fe^{III} ion in **1**.

A careful examination of the X- and Q-band spectra of **1** reveals that new lines are detected only for temperatures higher than 12 K. At the X band, they all increase in intensity upon increasing temperature, but two sets of lines can be distinguished from their temperature dependence. A first set at ≈600 and ≈650 mT superimpose between 45 and 65 K and decrease for higher temperatures. This temperature dependence strongly suggests that these lines originate from the S = 2 state (see Figure S3 in the SI). The second set of lines detected at the X band between 200 and 500 mT gain in intensity with increasing temperature and diminish for T higher than 70 or 80 K. This behavior indicates a main contribution from the S = 3 state. One would expect a similar temperature dependence at the Q band because this behavior is controlled by the Boltzmann population of the spin levels. A close inspection of the Q-band spectra reveals a continuous increase in the intensity of the signal located in the g_{eff} = 2 region (see Figure 7). This may result from a strong overlap of the S = 2 and 3 state signatures at the Q band.

The main features of the 9 and 34 GHz EPR spectra recorded at 15 or 20 K may be reproduced by assuming an axial ZFS within the S = 2 state with $|D_{S=2}| \approx 0.14$ cm^{-1}. However, line positions are not correctly reproduced simultaneously at both frequencies. This may be attributed to dipolar interactions because the X-band spectra recorded on a MeOH/toluene (1:1, v/v) solution of complex **1** show significant shifts of the transitions compared to the solid-state spectrum (see Figure S4 in the SI). Examination of the X-ray structure of complex **1** shows that two perchlorate counterions bridge two distinct $Fe^{III}Mn^{II}$ units through hydrogen bonding to the H_2O ligands (see Figure S5 in the SI). The separation between the two Mn^{II} ions is 9.454 Å and is the shortest intermolecular metal−metal distance. These hydrogen bonds may therefore act as an efficient relay for dipolar interactions between the two dinuclear units. Despite our efforts, no Q-band spectra could be recorded on solutions of **1**, precluding an accurate determination of the ZFS parameters of the S = 2 and 3 states.

Magnetic Properties of Compound 2. *NMR Spectroscopy.* The ^1H NMR spectrum of **2** in MeOH extends over ca. 200 ppm, from 183 to −17 ppm, and shows a number of well-resolved and relatively narrow signals (Figure 8). By contrast, that of **1** presents only very broad unresolved lines extending over ca. 100 ppm. This different behavior is due to the slow-relaxing properties of the Mn^{II} and Fe^{III} ions that induce a strong line broadening. On the other hand, the antiferromagnetic interaction is not strong enough to quench the electronic spin at room temperature. In complex **2**, the short electronic relaxation time of the Fe^{II} ion makes the overall system relax fast enough so that sharp NMR resonances are observed. Overall, the spectrum of **2** is highly similar to that of the $Fe^{II}Mn^{II}$ complex of the symmetrical tetrapyridyl complex,

dx.doi.org/10.1021/ic301725z | Inorg. Chem. 2012, 51, 10447−10460

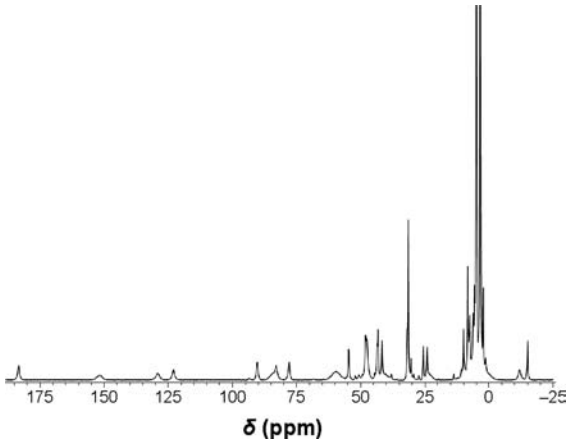

Figure 8. ^{1}H NMR spectrum of **2** in CD_3OD.

extending over the same 200 ppm scan range.[17] The spectrum of this complex presents two equally intense sharp resonances at −11.1 and −13.6 ppm, which are assigned to the two para protons of the manganese-bound pyridines. Interestingly, the spectrum of **2** presents a single resonance in this region. Owing to the fact that the Mn^{II} ion is highly isotropic, if it were bound to two pyridines, these two protons would resonate at similar fields. The observation of a single resonance can thus be taken as indicative that the manganese ion is bound by a single pyridine and that the two metal ions in **2** occupy the same location as that in **1**.

Magnetic Susceptibility. The $\chi_M T$ vs T curve for a powder sample of compound **2** is reproduced in Figure 5 (gray square points). At 300 K, the $\chi_M T$ value is 6.79 $cm^3 \cdot K \cdot mol^{-1}$, a value smaller than that of 7.375 $cm^3 \cdot K \cdot mol^{-1}$ expected for two noninteracting high-spin Fe^{II} ($S_{Fe} = 2$) and Mn^{II} ($S_{Mn} = {}^5/_2$) ions. Upon a decrease in the temperature, the $\chi_M T$ value decreases to 3.15 $cm^3 \cdot K \cdot mol^{-1}$ at 30 K. This behavior is characteristic of an antiferromagnetic interaction between the two metal ions. The data can be reproduced using the appropriate van Vleck formula with $J = 6.8(2)$ cm^{-1} ($\hat{H} = J\hat{S}_{Fe} \cdot \hat{S}_{Mn}$) and $g = 1.99(1)$ (gray solid line in Figure 5). The J value is similar to that measured for the single $Fe^{II}Mn^{II}$ complex published up to now, that is, 8 cm^{-1} in $[FeMn(bpmp)(\mu\text{-}O_2CCH_2CH_3)_2](BPh_4)$.[18] For this complex, the ZFS parameter $|D|$ was estimated to 5 cm^{-1}, suggesting that the iron ZFS and the exchange interaction may also be competitive in complex **2**.

EPR and Mössbauer Spectroscopies. The X-band EPR spectrum was recorded at 5 K on powder samples of **2** and is reproduced in Figure 9. An intense signal is detected between 250 and 650 mT. The profile and position suggest a nearly axial $S_{eff} = {}^1/_2$ species with g_{eff} factors mainly lower than 2. This signal decreases in intensity upon increasing temperature, demonstrating that it originates from the ground state. An $S = {}^1/_2$ ground state can indeed be achieved through the antiferromagnetic interaction between the high-spin Fe^{II} ($S_{Fe} = 2$) and Mn^{II} ($S_{Mn} = {}^5/_2$) ions evidenced by magnetic measurements. In addition, the temperature dependence of the signal intensity measured at 351 mT between 5 and 60 K (see Figure S6 in the SI) can be satisfyingly reproduced assuming that the signal originates from an $S = {}^1/_2$ ground state, with the S spin excited states lying at energies given by $JS(S + 1)/2$. The best fit leads to $J = 6.4(4)$ cm^{-1}, in fair agreement with the value obtained from the temperature dependence of the magnetic susceptibility.

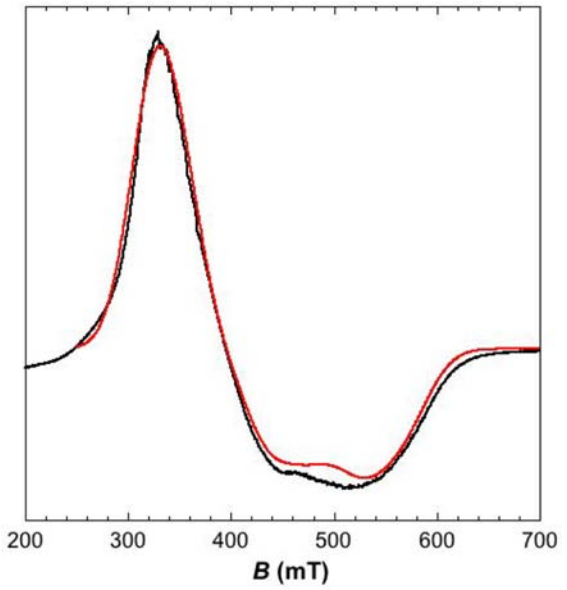

Figure 9. Experimental (solid black line) powder X-band EPR spectrum of **2** recorded at 5 K. The solid red line reproduces the theorical spectrum obtained from the simultaneous simulations of the EPR and Mössbauer spectra (parameters listed in Table 4).

Figure 10 reproduces the zero-field Mössabuer spectra (A and B top traces) recorded at 1.4 and 4.2 K on powder samples of **2**. They are indeed superimposable. A single quadrupole doublet is detected, in agreement with the unique location for the iron site evidenced by ^{1}H NMR investigations. In addition, the quadrupole splitting and isomer shift values are fully consistent with a high-spin Fe^{II} ion (see Table 4).

The Mössbauer spectra recorded at 1.4 and 4.2 K using a 4 or 7 T magnetic field applied parallel to the γ-rays are also shown in Figure 10 (C and D middle and E and F bottom traces, respectively). In order to fully determine the electronic structure of complex **2**, these four Mössbauer spectra were *simultaneously* simulated with the 5 K X-band EPR spectrum by considering the two $S_{Fe} = 2$ and $S_{Mn} = {}^5/_2$ spins in magnetic interaction. The Mn^{II} ion was assumed to be isotropic, that is, with no ZFS interaction and a single g_{Mn} factor that was fixed to 2.0. No dipolar coupling was included, with the two metal sites interacting only through the isotropic exchange interaction characterized by the J constant ($\hat{H} = J\hat{S}_{Fe} \cdot \hat{S}_{Mn}$). All of the electronic tensors (ZFS, hyperfine, and exchange) or matrices (electronic Zeeman) are coaxial but rotated with respect to the iron EFG tensor. The best simulations of the Mössbauer spectra were obtained assuming a slow relaxation regime. The obtained theoretical Mössbauer signatures are superimposed to the experimental traces as solid red lines for the 1.4 K spectra and as solid blue lines for the 4.2 K spectra (Figure 10). The resulting theoretical EPR spectrum is also shown as the solid red line in Figure 9. Parameter values are listed in Table 4. Only two out of three Euler angles are listed. The missing χ angle is associated with rotation about the z axis of the iron EFG tensor. Because the η parameter is found below 0.3, the iron EFG tensor is mainly axial and a rotation about the axis of distortion is not significant. The exchange J constant is fairly consistent with that determined from variation of the temperature of the $\chi_M T$ product and from the temperature dependence of the EPR intensity (6.8 and 6.4 cm^{-1}, respectively; see above). The D_{Fe} and J values are similar to those determined for the closely

dx.doi.org/10.1021/ic301725z | Inorg. Chem. 2012, 51, 10447−10460

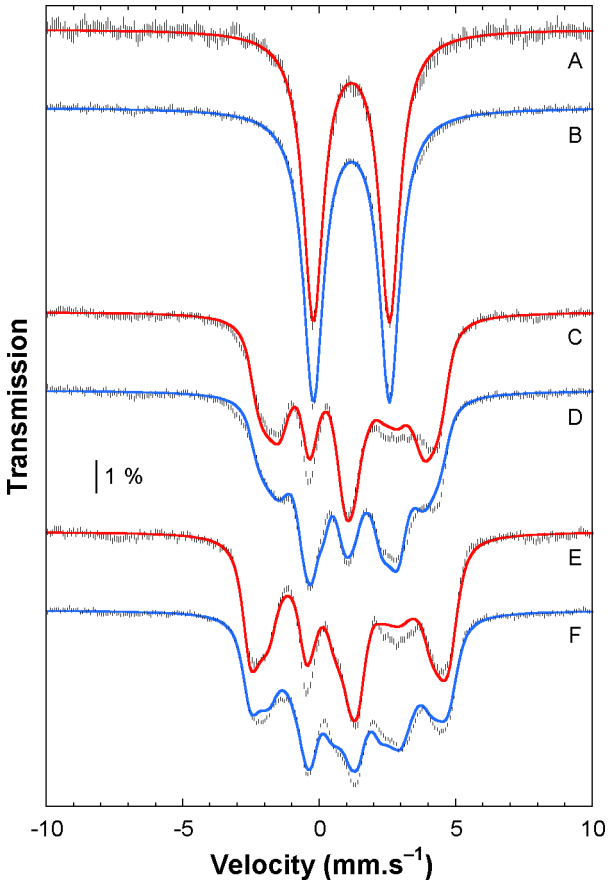

Figure 10. Experimental (dashed black lines) and simulated (solid red and blue lines) Mössbauer spectra recorded on a 100% ^{57}Fe-enriched powder sample of **2** at 1.4 K (traces A, C, and E) or 4.2 K (traces B, D, and F) at zero-field (A and B top traces) or with a 4 T (C and D middle traces) or 7 T (E and F bottom traces) external magnetic field applied parallel to the γ beam.

Table 4. Exchange Constant and Electronic and Nuclear Parameters for the Fe^{II} Site of Complex 2 Used for Simulating the Mössbauer and X-Band EPR Spectra[a]

J (cm^{-1})		5.72(15)	
g_{Fe} matrix	x	2.160(15)	
	y	2.194(10)	
	z	2.05(6)	
D_{Fe} (cm^{-1})		3.55(15)	
E_{Fe}/D_{Fe}		0.21(1)	
a_{Fe} tensor (T)	x	−23.1(20)	
	y	−5.8(10)	
	z	>−14.5	
$a_{Mn,iso}$ (10^{-4} cm^{-1})		96.3(20)	
ΔE_Q (mm·s^{-1})		2.80(6)	
η		<0.3	
Euler angles (deg)	ρ	61(10)	
	τ	59(9)	
δ (mm·s^{-1})		1.19(3)	
$\Gamma_{Möss}$ (mm·s^{-1})		0.28(3)	*0.45(2)*
Γ_{EPR} (MHz)		645	

[a]The manganese **g** matrix was set isotropically with $g_{Mn,iso}$ = 2. The line-width for the zero-field Mössbauer spectra is indicated in italics.

related complex [(bpmp)Fe^{II}(μ-O$_2$CCH$_2$CH$_3$)$_2$Mn^{II}](ClO$_4$) (|D_{Fe}| = 5 cm^{-1} and J = 8 cm^{-1}).[18] The intrinsic g_{Fe} matrix is, as expected, anisotropic with an isotropic component of 2.13 well in agreement with that determined for hexacoordinated Fe^{II} ions. The local iron hyperfine tensor is also highly anisotropic. Similar small eigenvalues were also obtained for the Fe^{II} site of dinuclear systems.[48,49] For instance, a value of −3.5 T was determined for one of the iron hyperfine components in [(tacn)Fe^{II}(μ-OH)(μ-OAc)$_2$Cr^{III}(tacn)](ClO$_4$)$_2$ (tacn = 1,4,7-triazacyclononane).[49]

Electronic Structure of the Ground State of 2. The Fe^{II}Mn^{II} pair has nine unpaired electrons. According to the Kramers theorem, this odd number leads at zero field to a degenerate ground state. In the strong exchange limit, that is, when the antiferromagnetic exchange interaction is dominant, one would expect the ground-state Kramers doublet to be the $S = {}^1/_2$ state and the first two excited-state Kramers doublets to be issued from the $S = {}^3/_2$ state. However, owing to the similar values of the D_{Fe} and J constants in **2**, this analysis within the strong exchange limit is not valid. The investigation of the composition of the lowest Kramers doublets indeed reveals a strong mixing between the states of total spin $S = {}^1/_2$, ${}^3/_2$, and ${}^5/_2$ (see eqs S1−S3 in the SI).

The procedure used to simulate the X-band EPR spectrum was checked by calculating the X-band EPR spectrum of compound **2** using the *XSophe* package where all of the EPR transitions within the dinuclear system are considered without any restriction. Taking the values of the electronic parameters listed in Table 4, the 1.4 K X-band EPR spectrum is indeed identical with the theoretical trace shown in Figure 9 (see Figure S7 in the SI). When the temperature is increased to 5 K, extra transitions appear below 250 mT and above 600 mT, without modifying the signal detected between (see Figure S7 in the SI). These additional transitions are issued from the first excited-state Kramers doublet. These calculations clearly demonstrate that the EPR signal detected between 250 and 600 mT only originates from the ground-state Kramers doublet and validate the whole calculation procedure that has been set up for the simulation.

To our knowledge, this is the first time that Mössbauer and EPR spectra are *simultaneously* simulated. A recent study on a μ-alkoxo-μ-carboxylato mixed-valent Fe^{II}Fe^{III} complex presents a detailed analysis of the electronic structure that relies on the analysis of both the EPR and Mössbauer spectra while shuttling back and forth between the two techniques.[50] The methodology relies on the weak ZFS of the Fe^{II} site—the one of the Fe^{III} is even weaker—which can be treated as a second-order perturbation of the exchange interaction. The obtained D and J constants (2.5 and 22.5 cm^{-1}, respectively) lead to a D/J ratio of 0.11. For complex **2**, this ratio reaches 0.62, precluding such an analysis. However, despite this high D/J ratio, it is remarkable to see that the ground-state Kramers doublet indeed behaves as a $S_{eff} = {}^1/_2$ system when small magnetic fields are applied.

Figure 11 reproduces the variations of the ground-state Kramers doublet energy levels when the magnetic field is applied along the principal directions of the iron ZFS tensor with a magnitude ranging from 0 to 8 T. The electronic parameters listed in Table 4 were used. A zoom of the 0−800 mT domain is shown in Figure S8 in the SI. For small magnetic fields such as those used in X-band recordings, linear variations are indeed observed, validating the hypothesis formulated for calculation of the 9 GHz EPR signature. It may be noticed that the slopes of the two levels are not the exact opposite of one another and slightly differ in absolute value. This is an

dx.doi.org/10.1021/ic301725z | Inorg. Chem. 2012, 51, 10447−10460

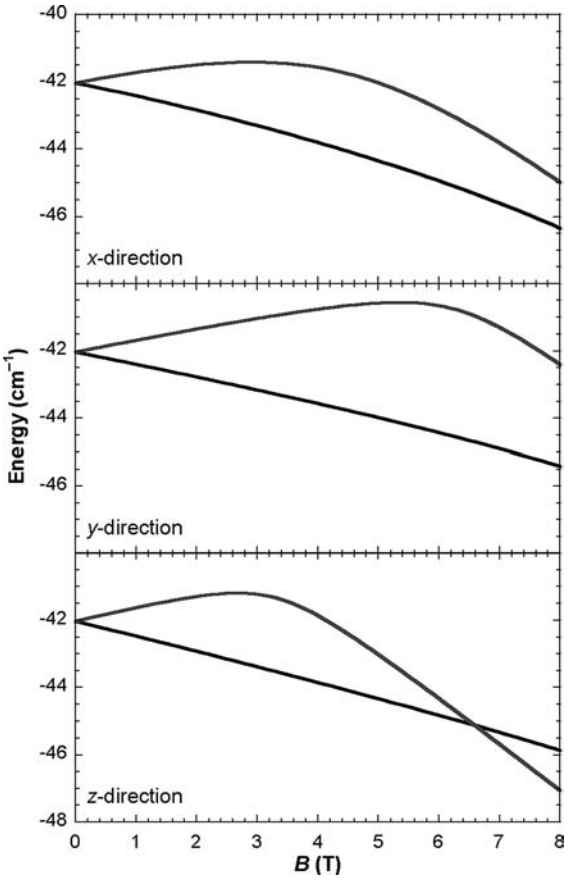

Figure 11. Variations upon the magnetic field B applied along the principal directions of the iron ZFS tensor of the energy of the two levels issued from the ground-state Kramers doublet, using the electronic parameters listed in Table 4.

indication that the ground-state Kramers doublet of **2** is not a pure $S_{eff} = {}^1/_2$ state because of the competitive iron ZFS and exchange interactions. These slopes allow determination of the average g_{eff} values that are listed in Table 5. The three principal values are smaller than 2, in agreement with the position of the EPR signal.

Table 5. Spin-Projection, g_{eff} and A_{eff} Values Calculated for the Ground-State Kramers Doublet of 2 Determined at Zero Field Using Electronic Parameters Listed in Table 4

		x direction	y direction	z direction
spin projections	Fe^{II}	∓0.550	∓1.250	∓0.190
	Mn^{II}	±0.968	±1.753	±0.650
g_{eff}		1.486	1.528	1.809
$A_{Mn,eff}$ (10^{-4} cm^{-1})		186.4	337.5	125.1

To reproduce the X-band EPR signature assuming a $S_{eff} = {}^1/_2$ system, one has also to determine the effective manganese hyperfine tensor. The manganese hyperfine interaction within the dinuclear complex **2** is reproduced by the Hamiltonian given in eq 6, where $\tilde{a}_{Mn}$ is the local manganese hyperfine tensor and $\hat{S}_{Mn}$ and $\hat{I}_{Mn}$ stand for the electronic and nuclear manganese spin operators, respectively.

$$\hat{H}_{hf,Mn} = \hat{S}_{Mn}\tilde{a}_{Mn}\hat{I}_{Mn} \quad (6)$$

The same manganese hyperfine interaction is simulated within a $S_{eff} = {}^1/_2$ system using the Hamiltonian given in eq 7, where $\tilde{A}_{Mn,eff}$ is the effective hyperfine tensor.

$$\hat{H}_{hf,Mn} = \hat{S}_{eff}\tilde{A}_{Mn,eff}\hat{I}_{Mn} \quad (7)$$

For the two Zeeman levels $|\varphi_\pm\rangle$ of the $S_{eff} = {}^1/_2$ system, one thus has the relation between the components of the effective and intrinsic hyperfine tensors ($k = x, y, z$; eq 8).

$$A_{Mn,eff,k} = a_{Mn,k}\frac{\langle\varphi_\pm|\hat{S}_{Mn,k}|\varphi_\pm\rangle}{\langle\varphi_\pm|\hat{S}_{eff}|\varphi_\pm\rangle} = \pm 2a_{Mn,k}\langle\varphi_\pm|\hat{S}_{Mn,k}|\varphi_\pm\rangle \quad (8)$$

Thus, an evaluation of the effective manganese hyperfine constants can be obtained based on the local manganese spin projections associated with the ground-state Kramers doublet. Calculations of the iron and manganese spin projections evidence no field dependence when the magnetic field ranges from 0 to 800 mT (see Figure S9 in the SI). The values are listed in Table 5 along with the effective manganese hyperfine constants. These were calculated according to eq 8 and assuming an isotropic local manganese hyperfine interaction with $a_{Mn,iso} = 96.3 \times 10^{-4}$ cm^{-1} (see Table 4). Attempts to resolve the manganese hyperfine interaction on frozen-solution EPR spectra unfortunately failed. The effective manganese hyperfine tensor is found to be highly anisotropic despite the local isotropic interaction. This is reminiscent of $Mn^{II}Mn^{III}$ systems, where the anisotropy on the Mn^{III} site due to the strong ZFS is transferred to the Mn^{II} site through the weak antiferromagnetic exchange interaction.[51]

The X-band EPR spectrum originating from the ground-state Kramers doublet considered as a $S_{eff} = {}^1/_2$ system is reproduced in Figure S10 in the SI. This theoretical trace is identical with that obtained by the simulation procedure. Consequently, for applied magnetic fields of less than 0.7 T, the ground state of compound **2** behaves as a $S_{eff} = {}^1/_2$ species. This is no longer true when stronger magnetic fields are applied.

Simulations of the 1.4 K Mössbauer spectra recording while applying a 4 or a 7 T magnetic field were performed assuming an $S_{eff} = {}^1/_2$ system. The g_{eff} values have been fixed to the values listed in Table 5. These two experimental spectra were equivalently reproduced by several sets of parameters (see Figure S11 in the SI for one typical result). These sets share in common an axial EFG tensor for Fe^{II}, in agreement with what was obtained when considering the dinuclear structure of complex **2** (see Table 4). All of the simulations also led to an iron hyperfine tensor presenting two positive principal values, with the third one being negative. Positive values are expected in the strong exchange limit because the Wigner−Eckart coefficient of the Fe^{II} site equals $-{}^4/_3$. The change in sign for one hyperfine component is a strong indication that the system deviates from a $S_{eff} = {}^1/_2$ system. Indeed, the separation between the two lowest Zeeman levels is weaker at 7 T than at 4 T (see Figure 11), while the separation continuously increases upon increasing field for a $S_{eff} = {}^1/_2$ system. In addition, the variations upon B of the first excited-state energy level clearly reveal an increasing $m_S = -{}^3/_2$ character, with this level even becoming the ground state for $B > 6.8$ T when the magnetic field is applied along the z direction. Note that the Fe^{II} site in the $S = {}^3/_2$ state has a positive Wigner−Eckart coefficient of $+{}^2/_{15}$ within the strong exchange limit. These facts demonstrate that, under high magnetic field, complex **2** can no longer be treated as a $S_{eff} = {}^1/_2$ species.

dx.doi.org/10.1021/ic301725z | Inorg. Chem. 2012, 51, 10447−10460

DISCUSSION

Metal Location. Iron and manganese have very similar coordination properties so finding which one is the physiological metal has proven difficult in many metalloproteins.[10] This difficulty has been highlighted recently in proteins possessing dinuclear active sites and is further enhanced with the recent discovery of new classes of redox-active enzymes with a heterodinuclear iron−manganese active site.[11,12] The question of the respective location of the two metal ions is crucial if one wants to understand the reactivity of these sites. Indeed, in R2lox it was shown that the iron and manganese ions are perfectly located in a single site, with the iron ion close to the tyrosine−valine link and the manganese ion at the entrance of the ligand-binding channel.[12] Similarly, in *C. trachomatis* RNR R2c cysteine oxidation by the Mn^{IV} site is relying on an electron-transfer pathway connecting the two redox-active sites, and the location of the manganese ion close to the phenylalanine that is in the position of the tyrosyl radical of the other RNR enzymes is therefore essential. Two recent articles have addressed this question through crystallographic and spectroscopic methods. From X-ray crystallography anomalous scattering experiments, Högbom et al.[52] concluded that the manganese ion occupies the position proximal to the otherwise tyrosyl-harboring radical site in other R2 proteins consistently, with the assumption that the high-valent Mn^{IV} species functions as a direct substitute for the tyrosyl radical. A similar conclusion was reached by Bollinger et al.,[53] but in-depth spectroscopic studies revealed that the alternate metal distibution and even a diiron form may be present.

Similar problems were encountered in the present study. Indeed, the unsymmetrical nature of the ligand and the similarity of its two binding sites make the problem of the preparation of an iron−manganese complex more difficult, with each metal fully occupying a single binding site as opposed to forming also homodinuclear pairs or scrambling over the two binding sites. The latter difficulty is not encountered with a symmetrical ligand[15,18] or one involving an anionic ligand that stabilizes the ferric ion.[20,22] Mössbauer spectroscopy illustrated this difficulty in revealing that the iron ions scrambled over the two binding sites in our initial attempts. The problem could be overcome for the $Fe^{III}Mn^{II}$ complex by careful monitoring of the metal quantities, and X-ray crystallography and Mössbauer spectroscopy concurred to show that the ferric ion occupies the binding site within the bis(picolylamine) branch. This localization of the two ions in **1** is quite in line with the previous results on the homodinuclear complexes,[24,26] which showed that the binding site with the bis(picolylamine) branch stabilizes the M^{III} ion, whether it is iron or manganese. This preference thus directs the metal binding in **1**. In the case of the reduced complex **2** with a $Fe^{II}Mn^{II}$ pair, no such preference exists and the higher similarity of the two ions complicated the synthesis and required the use of the sequential addition of carefully titrated solutions of each metal salt. Alternatively and preferably, **2** could be prepared from **1** by reduction with cobaltocene. It is interesting to note that the addition of an excess of the other metal ion to each of the homodinuclear complexes did not lead to metal replacement, showing that the metal ions in the dinuclear complexes are not labile.

Biological Relevance. It is clear from the above data that the magnetic properties of the iron−manganese species are governed by the J/D_{Fe} ratio. In the case of the strong exchange limit where $J \gg D$, spin states of the pair can be defined. Studies on homodinuclear systems have shown that this situation is currently met in oxo-bridged diferric species: the oxo bridge leads to a strong antiferromagnetic interaction ($J >$ 190 cm^{-1}), validating deconvolution of the EPR spectra into *S*-state signatures.[46] It can be met also occasionnally in certain dimanganese compounds where the *J* constant is weak ($J <$ 20 cm^{-1}) but sufficiently large to overwhelm the small ZFS interaction of the hexacoordinated Mn^{II} ions ($|D_{Mn}| <$ 0.1 cm^{-1}) and the dipolar coupling.[45] By contrast, a recent detailed investigation of a $[Fe^{III}(\mu\text{-}OMe)_2Fe^{III}]^{4+}$ core complex elegantly illustrated the deviation from the strong exchange limit. Compared to the single μ-oxo bridge, the two μ-methoxo groups reduce the antiferromagnetic interaction (J = 15.4 cm^{-1}), leading to a stronger influence of the Fe^{III} ZFS (D_{Fe} = 0.75 cm^{-1}) and consequently prohibiting a correct analysis of the EPR spectra within the strong exchange limit.[47]

In this respect, it is worth noting that an even higher *D* value (−1.5 cm^{-1}) was deduced for the Fe^{III} site of purple acid phosphatase from Mössbauer investigations.[48] Although the ZFS parameter of a hexacoordinated Fe^{III} ion is far weaker than that of Fe^{II}, it is possible that $Fe^{III}Mn^{II}$ species also depart from the strong exchange limit. On the other hand, the literature mentions a single determination of the exchange interaction for an iron−manganese protein, namely, the $Fe^{III}Mn^{II}$ form of purple acid phosphatase for which it was estimated to be higher than 140 cm^{-1}.[8] However, this value is not consistent with those determined for other related systems. Indeed, significantly smaller values were estimated for the $Fe^{II}Mn^{II}$ and $Fe^{III}Mn^{III}$ forms of *Escherichia coli* RNR, 2.6[54] and 36 cm^{-1},[55] respectively. The latter values are consistent with those obtained for the diiron forms of purple acid phosphatase of diverse origins (bovine spleen and red kidney bean purple acid phosphatases[56] and uteroferrin[57,58]) that span the range 6−35 cm^{-1}. These values were clearly associated with the occurrence of a hydroxo ion bridging the two metals. Similarly, all model complexes with a phenoxo bridge have an exchange interaction of the same order of magnitude, 13−23 cm^{-1} for the $Fe^{III}Mn^{II}$ complexes[15,18,20,22] and 8 ± 2 cm^{-1} for the only $Fe^{II}Mn^{II}$ complex[18] reported so far. In all of these systems, the exchange interaction is moderate at most. By contrast, when it was determined, the ZFS associated with the ferrous site exhibited rather strong values ranging from 5 to 11 cm^{-1}. Thus, the strong exchange limit situation was not met in these systems, as detailed for reduced uteroferrin[57,58] and for the $Fe^{II}Mn^{II}$ pair of the *E. coli* RNR.[54] It thus appears that the phenoxo-bridged model compounds possess electronic structures exhibiting competitive ZFS and exchange interaction similar to those of the corresponding protein active sites.

SUMMARY

In this Article, we described the synthesis and characterization of the electronic structures of two iron−manganese complexes of an unsymmetrical dinucleating ligand. Owing to the similarity of the two coordination sites and of the two metals involved, great care was required to obtain a single compound with a well-defined location of the two metals. This allowed the electronic structures of the $Fe^{II}Mn^{II}$ and $Fe^{III}Mn^{II}$ pairs to be studied with the help of EPR and Mössbauer spectroscopies. Characterization of the $Fe^{II}Mn^{II}$ center was of particular interest because this configuration is the one that reacts with dioxygen at the active site of *C. trachomatis* RNR. Owing to the similar values of the exchange interaction and the iron ZFS, extensive calculations were necessary to simulate both the EPR and

dx.doi.org/10.1021/ic301725z | *Inorg. Chem.* 2012, 51, 10447−10460

Mössbauer spectra. A similar situation was found in reduced uteroferrin[57,58] and the iron−manganese reconstituted form of *E. coli* RNR.[54] Accordingly, the present study is likely to be used as a reference for future spectroscopic work on these metal centers.

■ ASSOCIATED CONTENT

Supporting Information

Electronic composition in the $|S, m_S\rangle$ basis of the three lowest Kramers doublets of **2** determined at zero field using spin parameters listed in Table 4 (eqs S1−S3), ESI-MS spectrum of complex **2** (Figure S1), zoom of the $g = 2$ region of the 15 K Q-band EPR spectrum of **1** (Figure S2), temperature dependence of the contribution to the total EPR signature of the paramagnetic spin states of complex **1** (Figure S3), X-band EPR spectra recorded on powder and frozen solution samples of compound **1** (Figure S4), hydrogen-bound network between two $Fe^{III}Mn^{II}$ units within the crystal structure of **1** (Figure S5), temperature dependence of the X-band EPR signal of complex **2** at 351 mT measured between 5 and 60 K (Figure S6), theoretical X-band EPR spectrum issued from the simultaneous minimization of the EPR and Mössbauer spectra of compound **2** with the *XSophe* theoretical spectra calculated using the electronic parameters listed in Table 4 (Figure S7), zoom of the 0−800 mT domain of Figure 11 (Figure S8), variations of the Fe^{II} and Mn^{II} spin projections within compound **2** upon the external magnetic field applied along the *x*, *y*, and *z* principal directions of the iron ZFS tensor (Figure S9), theoretical X-band EPR spectrum issued from the simultaneous minimization of the EPR and Mössbauer spectra of compound **2** with that obtained while assuming a $S_{eff} = {}^1/_2$ species with parameters listed in Table 5 (Figure S10), and minimization of the 1.4 K magnetic Mössbauer spectra of **2** assuming a $S_{eff} = {}^1/_2$ species (Figure S11). This material is available free of charge via the Internet at http://pubs.acs.org.

■ AUTHOR INFORMATION

Corresponding Author

*E-mail: genevieve.blondin@cea.fr (G.B.), jean-marc.latour@cea.fr (J.-M.L.).

Notes

The authors declare no competing financial interest.

■ ACKNOWLEDGMENTS

The Région Rhône-Alpes (Grant CIBLE 07 016335) is gratefully acknowledged for its financial support. G.B. thanks Dr. Carole Duboc for her help in recording Q-band EPR spectra.

■ REFERENCES

(1) Stubbe, J.; Nocera, D. G.; Yee, C. S.; Chang, M. C. Y. *Chem. Rev.* **2003**, *103*, 2167.
(2) Nordlund, P.; Reichard, P. *Annu. Rev. Biochem.* **2006**, *75*, 681.
(3) Merkx, M.; Kopp, D. A.; Sazinsky, M. H.; Blazyk, J. L.; Müller, J.; Lippard, S. J. *Angew. Chem., Int. Ed.* **2001**, *40*, 2782.
(4) Sazinsky, M. H.; Lippard, S. J. *Acc. Chem. Res.* **2006**, *39*, 558.
(5) Shanklin, J.; Guy, J. E.; Mishra, G.; Lindqvist, Y. *J. Biol. Chem.* **2009**, *284*, 18559.
(6) Mitic, N.; Smith, S. J.; Neves, A.; Guddat, L. W.; Gahan, L. R.; Schenk, G. *Chem. Rev.* **2006**, *106*, 3338.
(7) Friedle, S.; Reisner, E.; Lippard, S. J. *Chem. Soc. Rev.* **2010**, *39*, 2768.
(8) Schenk, G.; Boutchard, C. L.; Carrington, L. E.; Noble, C. J.; Moubaraki, B.; Murray, K. S.; de Jersey, J.; Hanson, G. R.; Hamilton, S. *J. Biol. Chem.* **2001**, *276*, 19084.
(9) Schenk, G.; Gahan, L. R.; Carrington, L. E.; Mitic, N.; Valizadeh, M.; Hamilton, S. E.; de Jersey, J.; Guddat, L. W. *Proc. Natl. Acad. Sci. U.S.A.* **2005**, *102*, 273.
(10) Carboni, M.; Latour, J.-M. *Coord. Chem. Rev.* **2011**, *255*, 186.
(11) Jiang, W.; Yun, D.; Saleh, L.; Barr, E. W.; Xing, G.; Hoffart, L. M.; Maslak, M.-A.; Krebs, C.; Bollinger, J. M. J. *Science* **2007**, *316*, 1188.
(12) Andersson, C. S.; Högbom, M. *Proc. Natl. Acad. Sci. U.S.A.* **2009**, *106*, 5633.
(13) Borovik, A. S.; Que, L. J.; Papaefthymiou, V.; Münck, E.; Taylor, L. F.; Anderson, O. P. *J. Am. Chem. Soc.* **1988**, *110*, 1986.
(14) Bossek, U.; Weyhermüller, T.; Wieghardt, K.; Bonvoisin, J.; Girerd, J.-J. *J. Chem. Soc., Chem. Commun.* **1989**, 633.
(15) Buchanan, R. M.; Mashuta, M. S.; Richardson, J. F.; Oberhausen, K. J.; Hendrickson, D. N.; Webb, R. J.; Nanny, M. A. *Inorg. Chem.* **1990**, *29*, 1299.
(16) Hotzelmann, R.; Wieghardt, K.; Flörke, U.; Haupt, H.-J.; Weatherburn, D. C.; Bonvoisin, J.; Blondin, G.; Girerd, J.-J. *J. Am. Chem. Soc.* **1992**, *114*, 1681.
(17) Wang, Z.; Holman, T. R.; Que, L. J. *Magn. Reson. Chem.* **1993**, *31*, S78.
(18) Holman, T. R.; Wang, Z. G.; Hendrich, M. P.; Que, L. J. *Inorg. Chem.* **1995**, *34*, 134.
(19) Dutta, S. K.; Werner, R.; Flörke, U.; Mohanta, S.; Nanda, K. K.; Haase, W.; Nag, K. *Inorg. Chem.* **1996**, *35*, 2292.
(20) Karsten, P.; Neves, A.; Bortoluzzi, A. J.; Lanznaster, M.; Drago, V. *Inorg. Chem.* **2002**, *41*, 4624.
(21) Ross, S.; Weyhermüller, T.; Bill, E.; Bothe, E.; Flörke, U.; Wieghardt, K.; Chaudhuri, P. *Eur. J. Inorg. Chem.* **2004**, 984.
(22) Jarenmark, M.; Haukka, M.; Demeshko, S.; Tuczek, F.; Zuppiroli, L.; Meyer, F.; Nordlander, E. *Inorg. Chem.* **2011**, *50*, 3866.
(23) Lambert, E.; Chabut, B.; Chardon-Noblat, S.; Deronzier, A.; Chottard, G.; Bousseksou, A.; Tuchagues, J.-P.; Bardet, M.; Laugier, J.; Latour, J.-M. *J. Am. Chem. Soc.* **1997**, *119*, 9424.
(24) Kanda, W.; Moneta, W.; Bardet, M.; Bernard, E.; Debaecker, N.; Laugier, J.; Bousseksou, A.; Chardon-Noblat, S.; Latour, J.-M. *Angew. Chem., Int. Ed. Engl.* **1995**, *31*, 588.
(25) Chardon-Noblat, S.; Horner, O.; Chabut, B.; Avenier, F.; Debaecker, N.; Jones, P.; Pécaut, J.; Dubois, L.; Jeandey, C.; Oddou, J.-L.; Deronzier, A.; Latour, J.-M. *Inorg. Chem.* **2004**, *43*, 1638.
(26) Dubois, L.; Xiang, D.-F.; Tan, X.-S.; Pécaut, J.; Jones, P.; Baudron, S.; Le Pape, L.; Latour, J.-M.; Baffert, C.; Chardon-Noblat, S.; Collomb, M.-N.; Deronzier, A. *Inorg. Chem.* **2003**, *42*, 750.
(27) Dubois, L.; Caspar, R.; Jacquamet, L.; Petit, P.-E.; Charlot, M.-F.; Baffert, C.; Collomb, M.-N.; Deronzier, A.; Latour, J.-M. *Inorg. Chem.* **2003**, *42*, 4817.
(28) Avenier, F.; Dubois, L.; Dubourdeaux, P.; Latour, J.-M. *Chem. Commun.* **2005**, 480.
(29) *SMART and SAINT Area-Detector Control and Integration Software*; Bruker Analytical X-ray Instruments Inc.: Madison, WI, 1995.
(30) Sheldrick, G. M. *SHELXTL*, version 6.1; Bruker AXS Inc.: Madison, WI, 1997.
(31) Kahn, O. *Molecular Magnetism*; VCH: New York, 1993.
(32) Taylor, P. C.; Baugher, J. F.; Kriz, H. M. *Chem. Rev.* **1975**, *75*, 203.
(33) Pilbrow, J. R. *J. Magn. Reson.* **1984**, *58*, 186.
(34) Ben Haj Yedder, A. *Ec. Natl. Ponts Chaussées* **2002**.
(35) Rao, J. M.; Hughes, M. C.; Macero, D. J. *Inorg. Chim. Acta* **1976**, *18*, 127.
(36) Hughes, M. C.; Macero, D. J.; Rao, J. M. *Inorg. Chim. Acta* **1981**, *49*, 241.
(37) Sjödin, M.; Gätjens, J.; Tabares, L. C.; Thuéry, P.; Pecoraro, V. L.; Un, S. *Inorg. Chem.* **2008**, *47*, 2897.
(38) Romain, S.; Baffert, C.; Duboc, C.; Leprêtre, J.-C.; Deronzier, A.; Collomb, M.-N. *Inorg. Chem.* **2009**, *48*, 3125.

(39) Fox, B. G.; Hendrich, M. P.; Surerus, K. K.; Andersson, K. K.; Froland, W. A.; Lipscomb, J. D.; Münck, E. *J. Am. Chem. Soc.* **1993**, *115*, 3688.
(40) Hendrich, M. P.; Day, E. P.; Wang, C.-P.; Synder, B. S.; Holm, R. H.; Münck, E. *Inorg. Chem.* **1994**, *33*, 2848.
(41) Kauffmann, K. E.; Popescu, C. V.; Dong, Y.; Lipscomb, J. D.; Que, L. J.; Münck, E. *J. Am. Chem. Soc.* **1998**, *120*, 8739.
(42) Schünemann, V.; Paulsen, H. In *Applications of Physical Methods to Inorganic and Bioinorganic Chemistry*; Scott, R. A., Ed.; Wiley: New York, 2007; p 243.
(43) Semenaka, V. V.; Nesterova, O. V.; Kokozay, V. N.; Dyakonenko, V. V.; Zubatyuk, R. I.; Shishkin, O. V.; Boca, R.; Jezierska, J.; Ozarowski, A. *Inorg. Chem.* **2010**, *49*, 5460.
(44) Sorace, L.; Golze, C.; Gatteschi, D.; Bencini, A.; Roesky, H. W.; Chai, J.; Stuckl, A. C. *Inorg. Chem.* **2006**, *45*, 395.
(45) Blanchard, S.; Blain, G.; Rivière, E.; Nierlich, M.; Blondin, G. *Chem.—Eur. J.* **2003**, *9*, 4260.
(46) Ozarowski, A.; McGarvey, B. R.; Drake, J. E. *Inorg. Chem.* **1995**, *34*, 5558.
(47) ter Heerdt, P.; Stefan, M.; Goovaerts, E.; Caneschi, A.; Cornia, A. *J. Magn. Reson.* **2006**, *179*, 29.
(48) Sage, J. T.; Xia, Y.-M.; Debrunner, P. G.; Keough, D. T.; de Jersey, J.; Zerner, B. *J. Am. Chem. Soc.* **1989**, *111*, 7239.
(49) Rodriguez, J. H.; Xia, Y. M.; Debrunner, P. G.; Chaudhuri, P.; Wieghardt, K. *J. Am. Chem. Soc.* **1996**, *118*, 7542.
(50) Li, F.; Chakrabarti, M.; Yanhong, D.; Kauffmann, K. E.; Bominaar, E. L.; Münck, E.; Que, L. J. *Inorg. Chem.* **2012**, *51*, 2917.
(51) Zheng, M.; Khangulov, S. V.; Dismukes, C. G.; Barynin, V. V. *Inorg. Chem.* **1994**, *33*, 382.
(52) Andersson, C. S.; Öhrström, M.; Popovic-Bijelic, A.; Gräslund, A.; Stenmark, P.; Högbom, M. *J. Am. Chem. Soc.* **2012**, *134*, 123.
(53) Dassama, L. M. K.; Boal, A. K.; Krebs, C.; Rosenzweig, A. C.; Bollinger, J. M. J. *J. Am. Chem. Soc.* **2012**, *134*, 2520.
(54) Pierce, B. S.; Hendrich, M. P. *J. Am. Chem. Soc.* **2005**, *127*, 3613.
(55) Pierce, B. S.; Elgren, T. E.; Hendrich, M. P. *J. Am. Chem. Soc.* **2003**, *125*, 8748.
(56) Gehring, S.; Fleischhauer, P.; Behlendorf, M.; Hüber, M.; Lorösch, J.; Haase, W.; Dietrich, M.; Witzel, H.; Löcke, R.; Krebs, B. *Inorg. Chim. Acta* **1996**, *252*, 13.
(57) Rodriguez, J. H.; Ok, H. N.; Xia, Y. M.; Debrunner, P. G.; Hinrichs, B. E.; Meyer, T.; Packard, N. H. *J. Phys. Chem.* **1996**, *100*, 6849.
(58) Day, E. P.; David, S. S.; Peterson, J.; Dunham, W. R.; Bonvoisin, J. J.; Sands, R. H.; Que, J. L. *J. Biol. Chem.* **1988**, *263*, 15561.